Title

Optogenetic actin network assembly on lipid bilayer uncovers the network density-dependent functions of actin-binding proteins.

Author list

Kei Yamamoto[1*], and Makito Miyazaki[1,2,3*]

Affiliations

[1]RIKEN Center for Biosystems Dynamics Research, 1-7-22 Suehiro-cho, Tsurumi-ku, Yokohama 230-0045, Japan.

[2]Graduate School of Medicine, Science and Technology, Shinshu University, 3-1-1 Asahi, Matsumoto, Nagano 390-8621, Japan.

[3]PRESTO, JST, 4-1-8 Honcho, Kawaguchi, Saitama, 332-0012, Japan.

*Correspondence: kei.yamamoto.jv@riken.jp and makito.miyazaki@riken.jp

Abstract

The actin cytoskeleton forms a mesh-like network that drives cellular deformations. The network property is defined by the network density and the species of the actin-binding proteins. However, the relationship between the actin network density, the penetration ability of actin-binding proteins into the network, and resulting network dynamics remains elusive. Here, we report an *in vitro* optogenetic system, named OptoVCA, which induces Arp2/3-mediated actin network assembly on a lipid membrane. By changing the illumination power, duration, and pattern, the OptoVCA flexibly manipulates the density, thickness, and shape of the actin network. Taking these advantages, we examine the effects of the network density on the two representative actin-binding proteins, myosin and ADF/cofilin. We find that the penetration of myosin filaments into the network is strictly inhibited by only a several-fold increase in network density due to the steric hindrance. Furthermore, penetrated myosin filaments induce directional actin flow when the network has a density gradient. On the other hand, ADF/cofilin penetrates into the network regardless of network density, however, network disassembly is dramatically inhibited by only a several-fold increase in network density. Thus, the OptoVCA contributes to understanding cell mechanics through the examination of the network density-dependent effect on the actin-binding proteins.

Introduction

The mesh-like actin network is a ubiquitous structure of the actin cytoskeleton, playing pivotal roles in dynamic cellular deformations such as a lamellipodium, bleb, and contractile ring (Kadzik, Homa, and Kovar 2020; García-Arcos et al. 2024). The network properties that characterize the specific subcellular structures are determined through interactions between actin filaments (F-actin) and actin-binding proteins (ABPs) related to each structure (Svitkina 2018; Blanchoin et al. 2014; Clarke and Martin 2021; Pollard 2016). To initiate the actin network assembly, actin polymerization is triggered by various nucleation-promoting factors (NPFs). The Wiskott-Aldrich syndrome protein (WASP) and WASP-family verprolin-homologous protein (WAVE) are the two major NPFs that activate a nucleator, the Arp2/3 complex, which in turn initiates branching of F-actin (Kurisu and Takenawa 2009; Derivery and Gautreau 2010; Firat-Karalar and Welch 2011). These NPFs are activated on lipid membranes including plasma membranes and organelle surfaces, and control the actin network assembly (Alekhina, Burstein, and Billadeau 2017; Breitsprecher and Goode 2013). During and after the actin network assembly, various ABPs interact with the network. Among ABPs, myosin II is a primary force generator that induces cellular deformations by generating contractile force with F-actin (Vicente-Manzanares et al. 2009; Craig and Woodhead 2006). ADF/cofilin (hereafter referred to as cofilin) disassembles the actin network by severing actin filaments, releasing the mechanical stress and enabling the dynamic recycling of F-actin (Bravo-Cordero et al. 2013).

Recent studies suggest that not only the species of ABPs but also tight regulation of the actin network density is important to achieve cellular functions. For example, it has been reported that myosin motors cannot generate proper contractile force both in sparse and dense actin networks in mammalian culture cells (Chugh et al. 2017). In addition, it has been reported that the penetration ability of ABPs into the actin network is affected by their protein sizes; smaller proteins such as ERM family proteins can enter the network, while larger proteins such as myosin filaments are frequently observed at the interior side of the cortical actin network (Truong Quang et al. 2021). Another potential function of the actin network is to serve as a steric barrier for proper organelle distributions in the cytoplasm (Moore et al. 2021; Olguin-Olguin et al. 2021). This growing evidence supports the idea that the actin network density is one of the key factors that broadly regulates not only the cell mechanics but also cellular functions mediated by ABPs and organelles. However, it is technically difficult to address the relationship between the protein sizes, the actin network densities, and the resulting functions of ABPs using live cells because of the complexity, thinness, and dynamicity of the actin networks (Laplaud et al. 2021; Jawahar et al. 2024).

To understand how the interactions between the actin network and ABPs are self-organized into specific structures, recent efforts have been devoted to reconstituting the actin cytoskeleton *in*

68 *vitro*. The patterned illumination of UV light to a PEG-coated glass enables the binding of NPFs in
69 the specified regions (Boujemaa-Paterski et al. 2017; Manhart et al. 2019; Bieling et al. 2016; Anne-
70 Cécile Reymann et al. 2010, 2012). These studies have elucidated the characteristics of actin networks
71 resulting from the various distributions and densities of NPFs on the substrates. Recently, the
72 techniques to bind NPFs on a spatially patterned lipid bilayer have been developed, making it possible
73 to analyze actin dynamics in more biologically relevant conditions (Colin et al. 2023; Yamazaki et al.
74 2024). However, it is still technically challenging to control actin polymerization in both space and
75 time. Moreover, it is also difficult to assemble actin networks with various densities on the same lipid
76 surface. Hence, further flexibility for the control of actin polymerization in the reconstituted systems
77 has been desired.

78 Here, we develop an *in vitro* optogenetic system that allows us to control the actin network
79 densities, thicknesses, and shapes with high temporal and spatial resolutions on a lipid bilayer. First,
80 as a proof of concept, we use mammalian culture cells and show that the actin cortex is formed by
81 light-induced recruitment of the VCA domain of WAVE1 to the plasma membrane. Actin
82 polymerization induced by our system, named OptoVCA, is an Arp2/3-dependent manner. Next, we
83 expand this strategy for *in vitro* experiments by combining OptoVCA with a mixture of purified actin
84 cytoskeletal proteins and a supported lipid bilayer (SLB). Using this system, we demonstrate that the
85 penetration ability of ABPs into the actin network and functions of ABPs are tightly regulated by the
86 network density and the size of ABPs. These observations highlight the importance of the actin
87 network density to understand cell mechanics.

Results

Optogenetic manipulation of actin polymerization in live cells.

To control the assembly of actin networks by light illumination, we used WAVE1, one of the major NPFs in mammalian cells. WAVE1 contains the V domain and CA domain, which interact with G-actin and Arp2/3, respectively. These domains are collectively called the VCA domain (Kurisu and Takenawa 2009) (Fig. 1a). WAVE1 is inactivated by the WAVE regulatory complex (WRC). When WRC is recruited to the plasma membrane through the interactions with Rac1, PIP_3, and IRSp53, the VCA domain is exposed to the cytoplasm. The activated WAVE1 recruits G-actin and Arp2/3 to the VCA domain and promotes actin nucleation, leading to actin polymerization. In line with this molecular mechanism, it has been reported that artificially localized VCA domain to the actin cortex induces cortical thickening in mouse oocytes (Chaigne et al. 2015). Light-induced oligomerization or membrane targeting of NPFs also enables control of actin polymerization (Nakamura et al. 2023; Taslimi et al. 2014). Therefore, we expected that a light-induced local increase in the density of the VCA domain would be sufficient for promoting actin polymerization both *in vivo* and *in vitro*. To test this idea, we first used mammalian culture cells (Madin-Darby Canine Kidney; MDCK cells), which contain all the components necessary for actin polymerization. As an optogenetic switch, we employed an improved Light-Induced Dimer (iLID) system, in which iLID and SspB bind together upon blue light illumination and reversibly dissociate under dark conditions (Guntas et al. 2015).

To manipulate the intracellular localization of the VCA domain and to increase its local density on the plasma membrane, we expressed iLID fused with stargazin (Yamamoto et al. 2021; Natwick and Collins 2021) and SspB fused with the VCA domain (hereafter referred to as the OptoVCA; Fig. 1a, S1a). Each fusion protein was visualized using mEGFP or mScarlet-I, respectively. To evaluate the effect of the translocation of the VCA domain on the cortical F-actin dynamics, we used MDCK cells expressing Lifeact-miRFP703 and Stargazin-mEGFP-iLID immediately after the trypsinization. SspB-mScarlet-I-VCA or SspB-mScarlet-I were also co-expressed as OptoVCA and the control, respectively. As a result, both SspB-mScarlet-I-VCA and SspB-mScarlet-I translocated from the cytoplasm to the plasma membrane upon blue light illumination (Fig. 1b, 1c, S1b). On the other hand, the cortical fluorescence intensity of Lifeact-miRFP703 was increased only in the cells expressing SspB-mScarlet-I-VCA and reached a nearly steady state within ~2 min (Fig. 1b, 1d, S1c). After stopping the illumination, both the SspB and Lifeact signals returned to the basal levels within ~4 min. These results demonstrate that the OptoVCA system can rapidly and reversibly control actin polymerization and depolymerization.

In these experiments, we transiently expressed Stargazin-mEGFP-iLID and SspB-mScarlet-I-VCA. Consequently, the expression ratio of these optogenetic proteins and the expression level of

122 SspB-mScarlet-I-VCA varied among the cells. To clarify the relationship between the expression
123 level and the translocation efficiency of the SspB-mScarlet-I-VCA, and the resulting actin
124 polymerization, we analyzed these parameters in each cell. The result shows that the cells with higher
125 expression levels and translocation efficiency positively correlate with a higher increase in F-actin
126 fluorescence (Fig. 1e). This further supports the significance of the local increase in the VCA density
127 for efficient actin polymerization.
128 Finally, we confirmed that this actin polymerization is mediated by Arp2/3; the cells treated
129 with CK-666, an Arp2/3 inhibitor, showed a relatively weaker increase in the cortical Lifeact signal
130 compared to the DMSO-treated control cells during illumination (Fig. 1f, 1g), although the
131 translocation dynamics of SspB-mScarlet-I-VCA were nearly identical between the two conditions
132 (Fig. S1e). In addition, we frequently observed wavy shape changes in the cells expressing OptoVCA
133 upon illumination (Fig. S1f). This result is consistent with the previous report showing that artificially
134 localized VCA domain to the actin cortex softens and deforms mouse oocytes (Chaigne et al. 2015).
135 Collectively, these results show that the OptoVCA system can control actin polymerization by
136 activating Arp2/3 with blue light.
137
138
139 **Optogenetic manipulation of actin polymerization on a supported lipid bilayer.**
140 Next, we expanded this optogenetic approach to an *in vitro* reconstitution system. We combined the
141 OptoVCA with a supported lipid bilayer (SLB), and reconstructed a biologically relevant actin
142 network from purified proteins on the lipid membrane. As for the SLB, we used POPC as the main
143 component and added 2-6% of DGS-NTA(Ni) to anchor His-mEGFP-iLID on the SLB (Fig. S2a).
144 The smoothness of the SLB was confirmed by the fluorescence signals of Marina Blue-conjugated
145 phospholipids and His-mEGFP-iLID attached to the membrane after forming the SLB (Fig. S2b).
146 The fluidity of the SLB was also confirmed by observing the lateral Brownian motion of single His-
147 mEGFP-iLID molecules along the membrane using TIRF microscopy (Fig. S2c). The density of His-
148 mEGFP-iLID on the SLB was controllable by changing the percentage of DGS-NTA(Ni) in the SLB
149 (Fig. S2d, S2e). We next examined if flavin mononucleotide (FMN) is needed as a chromophore for
150 iLID (Guntas et al. 2015). We loaded SspB-mScarlet-I-VCA to the His-mEGFP-iLID bound on the
151 SLB in the presence of various FMN concentrations, then we illuminated a 37 × 37 μm square pattern
152 of blue light at each condition and quantified the fluorescence intensities of SspB-mScarlet-I-VCA
153 recruited on the SLB. Notably, the addition of >1 μM FMN dramatically improved the translocation
154 efficiency of SspB-mScarlet-VCA to the SLB (Fig. S2f, S2g, S2h). Therefore, we added 10 μM FMN
155 in the following experiments.

To induce actin network assembly by blue light illumination, we added actin, profilin, Arp2/3, and capping protein (CP) to the OptoVCA. The cytoskeletal protein components were chosen according to the previous reports (Boujemaa-Paterski et al. 2017; Bieling et al. 2016; Dürre et al. 2018) (Fig. 2a). Before conducting the reconstitution experiments, we measured the actin polymerization activity of the purified proteins by the pyrene fluorescence assay (Fig. S3a), and confirmed that the polymerization activity is not affected by the addition of FMN or His-mEGFP-iLID, but is dependent on the presence of SspB-mScarlet-I-VCA and Arp2/3. Upon blue light illumination, SspB-mScarlet-I-VCA was rapidly recruited to the lipid surface, with the density nearly proportional to the percentage of DGS-NTA(Ni) in the SLB (Fig. 2b, 2d, S3b). Subsequently, actin polymerization started in the illuminated region (Fig. 2b, 2e, S3b). Notably, actin polymerization on the 6% DGS-NTA(Ni) lipid initiated much faster than that on the 2% DGS-NTA(Ni) lipid; the visible polymerization started within 1 min (Fig. 2c, 2e). After starting the polymerization on the 6% DGS-NTA(Ni) lipid, the fluorescence intensity of actin increased transiently and then decreased near the bottom plane close to the SLB (Fig. 2e). This phenomenon can be attributed to the local monomer depletion effect around the illuminated region; the higher the VCA density on the SLB, the more monomer actin and ABPs are recruited to the SLB, leading to a decrease in the surrounding protein concentrations (Boujemaa-Paterski et al. 2017; Manhart et al. 2019; Dimchev et al. 2017). On the other hand, the slower increase in actin density on the 2% DGS-NTA(Ni) lipid suggests a weaker effect of local monomer depletion (Fig. 2e, S3b). During illumination, the polymerized actin gradually formed a cup-like or dome-like structure on the 2% and 6% DGS-NTA(Ni) lipid, respectively (Fig. 2c, S3c).

To characterize the temporal resolution of the *in vitro* OptoVCA system, we examined how quickly actin polymerization halts after stopping the illumination. We illuminated the 6% DGS-NTA(Ni) lipid for 10, 20, or 30 min with a 37 × 37 μm square pattern. After stopping the illumination, the fluorescence intensity of SspB-mScarlet-I-VCA rapidly decreased (Fig. 2f), while the fluorescence intensity of actin gradually decreased in the case of 10 or 20 min illumination (Fig. 2g). This may be caused by the collapse of the actin network (i.e. debranching of Arp2/3-mediated branches (Le Clainche, Pantaloni, and Carlier 2003)), which occurs preferentially from the bottom plane because the bottom plane exhibits a lower actin density due to the local monomer depletion effect. In the absence of Arp2/3, actin fluorescence was nearly undetectable, even though SspB-mScarlet-I-VCA remained on the SLB by continuous illumination. This clarified that actin polymerization in the *in vitro* OptoVCA system is also mediated by Arp2/3 (Fig. 2f, 2g). We next focused on the growth dynamics of the actin pillar. While actin pillars continued to grow under constant light illumination, the growth ceased immediately after stopping the illumination, showing that *in vitro* OptoVCA system can precisely control the thickness of actin pillars (Fig. 2h). By

191 changing the illumination pattern over time, the more complex actin structures were also freely
192 designed (Fig. S3d, S3e, Movie S1). Furthermore, to dissect the initiation process of the actin network
193 assembly, we observed the growth of polymerized actin with high-speed imaging. We found that
194 actin clusters appeared on the SLB within 20 sec, then gradually expanded and fused with each other
195 (Fig. 2i, 2j, Movie S2). Considering that the nucleation process requires a mother actin filament,
196 Arp2/3, and the VCA domain, this observation suggests that the nucleation is initiated by the binding
197 of diffusing F-actin fragments stochastically nucleated in the bulk region to the complex of Arp2/3
198 and two VCA domains formed on the SLB (Gautreau et al. 2022; Espinoza-Sanchez et al. 2018).
199 Collectively, these results demonstrate that the optimized setup of the OptoVCA system enables
200 flexible control of actin polymerization in both spatial and temporal manners *in vitro*.
201
202
203 **Control of the actin network density by the light intensity.**
204 To quantify the relationship between the local density of the VCA domain on the SLB and the
205 resulting density of the actin network, we next examined whether our system can control the
206 efficiency of SspB-mScarlet-I-VCA recruitment by varying the light intensity. Given the high
207 sensitivity of the LOV domain used as a light-responsive protein in iLID (Berlew et al. 2022), we
208 reduced the light intensity to ~1% by inserting an ND filter into the light path of our microscope. We
209 confirmed that the exact light intensity emitted from the objective lens was linearly associated with
210 the output power controlled by the microscope software (Fig. S4a, S4b). By illuminating 37 × 37 μm
211 square patterns of blue light with varied intensities to the 6% DGS-NTA(Ni) lipid, we found that the
212 efficiency of SspB-mScarlet-I-VCA recruitment was almost saturated at the intensity with 0.35% of
213 the original maximum output (Fig. 3b, 3c, Movie S3). On the other hand, we observed reduced
214 recruitment of SspB-mScarlet-I-VCA at outputs of less than 0.35%. Consistent with this, the densities
215 of polymerized actin were nearly proportional to the densities of SspB-mScarlet-I-VCA on the SLB
216 when the outputs were smaller than 0.35% (Fig. 3d, 3e). The fluorescence intensity of actin pillars
217 assembled with an output greater than 0.25% started to decrease 10 min after starting the illumination,
218 presumably due to the local monomer depletion effect (Fig. 3d). The growth rate of actin pillars
219 formed under the strong illumination was slower than that formed under the weak illumination (Fig.
220 3a, S4c). This result can be explained by the balance between the local VCA density on the SLB and
221 the supply of actin monomers and ABPs from outside the pillars; if it is assumed that the supply of
222 actin monomers and ABPs is homogenous around the pillars, the higher local VCA density consumes
223 more actin monomers and ABPs, resulting in slower growth. In addition, we noticed that the top of
224 the pillars showed curved edges when illuminated with 0.35-0.45% or without using the ND filter
225 (Fig. 2c, 3a). The curved edges would be formed because of the leak of SspB-mScarlet-I-VCA to the

226 outside of the illuminated region by its lateral diffusion on the SLB. Overall, our system can precisely
227 manipulate the actin network density by controlling the recruitment of SspB-mScarlet-I-VCA to the
228 SLB through variations in light intensity.
229
230
231 **Actin density-dependent penetration of myosin filaments into the network.**
232 Next, we applied the OptoVCA system to understand the relationship between the density of the actin
233 network, the size of ABPs, and their penetration ability into the network. In living cells, it has been
234 suggested that the penetration of myosin filaments into the cortical actin network is crucial for
235 generating proper contractile force (Truong Quang et al. 2021). Therefore, we first chose myosin II
236 as a representative ABP and examined to what extent the actin network density impacts the myosin
237 penetration ability and the network deformability. Myosin molecules assemble into filaments through
238 the phosphorylation of their light chains (Craig and Woodhead 2006). Prior to the experiments,
239 smooth muscle myosin (SMM) was phosphorylated by ZIP kinase to induce filament formation and
240 activation of motor activity (Komatsu and Ikebe 2004; Murata-Hori et al. 1999). The length of myosin
241 filaments was 1.32 ± 0.66 μm (mean ± SD; Fig. S5a, S5b). To examine the effects of actin network
242 density on myosin distributions, we mixed the preformed myosin filaments with the other components,
243 and then induced the formation of actin networks with various densities. Interestingly, while the
244 myosin signal was detected within the sparse actin network assembled with 0.05% output, most of
245 the myosin signal was detected on the surface of the dense actin networks assembled with 0.15% and
246 0.35% outputs (Fig. 4a, middle column, S5c). This result indicates that the actin network density
247 determines the efficiency of myosin filament penetration into the network. Strikingly, only a ~2.5-
248 fold increase of the actin network density almost completely inhibits penetration of myosin filaments
249 in an all-or-none fashion (Fig. 4a, middle column, Fig. 4b). To further explore the network density
250 effect, we formed a sparser network by reducing the concentrations of actin and ABPs in the system
251 (Fig. 4a, right column, 4b). As expected, in the sparse condition, the myosin signal was detected in
252 the network even under illumination with 0.15% and 0.35% outputs. Notably, the myosin and actin
253 signals in the sparse conditions were mutually exclusive (Fig. 4c). Next, we asked whether the
254 penetration ability of myosin filaments is dependent on only the actin network density or also on the
255 ATPase activity of myosin motors. To examine this, we treated myosin filaments with blebbistatin, a
256 myosin ATPase inhibitor (Straight et al. 2003), and compared the myosin signal intensity inside the
257 actin networks with control conditions (Fig. S5d). In the networks assembled with 0.15% and 0.35%
258 outputs, the myosin signal was significantly weaker in the blebbistatin-treated condition than in the
259 control condition (Fig. S5e, S5f). These results provide direct evidence that both a sparse actin

network and myosin with ATPase activity contribute to the efficient penetration of myosin filaments into the actin network.

Next, we evaluated how the network density impacts the deformability. Interestingly, after stopping the illumination with 0.05% output in the sparse condition, the actin and myosin puncta were rapidly concentrated and formed a large cluster (Fig. 4d). This is consistent with the previous observations regarding the formation of actomyosin condensates in *in vitro* systems and living cells (Soares e Silva et al. 2011; Kruse et al. 2024). Such condensates were not formed in the dense networks, suggesting that the network deformability is determined by the penetration ability of myosin filaments. In living cells, myosin-driven network deformations are frequently observed as a cortical flow during migration and cytokinesis (Kelkar, Bohec, and Charras 2020; Paluch, Aspalter, and Sixt 2016). However, the causal relationship between the actin network density and the direction of the cortical flow has not been explicitly demonstrated due to the complexity of living cells. To examine the direct role of the network density in the actin flow, we assembled the actin network having a density gradient by changing the illumination power in space (Fig. 4e). To obtain a thin deformable actin sheet, we illuminated the SLB for 1-2 min. In the absence of myosin, we confirmed that the actin sheet remained at the same position on the SLB for at least 24 min after stopping the illumination (Fig. 4f, 4h). In the presence of myosin, actin and myosin started contraction and concentrated toward the densest network region immediately after stopping the illumination (Fig. 4g, 4h, Movie S4). The fluorescence intensity of myosin decreased over time in the regions illuminated with 0.05% and 0.15% outputs, whereas it increased in the region illuminated with 0.35% output, indicating that myosin filaments were transported toward the densest network region by unidirectional actin flow (Fig. 4i). To further demonstrate that the flow direction can be determined solely by the network density gradient, we illuminated strong light in the center region of the SLB and formed actin density gradients along both sides (Fig. 4j). As a result, the actin sheet showed flows toward the center, further supporting that the actin density gradient determines the flow direction (Fig. 4k, Movie S5). Moreover, we found that F-actin in the sparsest regions on both sides was not connected to the network and was freely floating (Fig. 4k). These results provide direct evidence that only the actin density gradient and the network connectivity are sufficient factors to induce the directed actin flow by myosin.

Actin density-dependent disassembly of the network by cofilin.

To examine the effect of relatively smaller-sized ABPs on the actin network, next we focused on cofilin, an actin depolymerization factor, with ~3.5 nm in diameter (Tanaka et al. 2018; Huehn et al. 2020). We illuminated the SLB with five different outputs to assemble actin networks with different

295 densities, and then monitored the network disassembly dynamics after stopping the illuminations both
296 in dense and sparse conditions (Fig. 5a, 5b). For simplicity, blue light was illuminated only for 10
297 min to avoid the local monomer depletion effect. We quantified the actin network disassembly level
298 in various network densities by calculating the ratio of the fluorescence intensities of actin before and
299 10 min after stopping the illuminations. Interestingly, the network disassembly level sharply
300 decreased as the network density increased, showing that the cofilin-mediated network disassembly
301 dramatically suppressed in dense actin networks (Fig. 5c). In addition, we found that the actin density
302 just after stopping the illumination was nearly identical regardless of cofilin concentrations in the
303 dense condition, while it was decreased with increasing cofilin concentrations in the sparse condition
304 (Fig. S6a, S6b). These results are consistent with the previous report that the network disassembly is
305 inversely proportional to the square of the local actin density and proportional to the actin-bound
306 cofilin density (Manhart et al. 2019).

307 Why is the cofilin-mediated network disassembly suppressed in dense actin networks? We
308 hypothesized that the accessibility of cofilin to the actin pillar is sterically hindered by the network
309 density at a specific threshold, as seen in myosin filaments. To test this hypothesis, we first estimated
310 the actin network density by comparing the fluorescence intensities of actin in the pillars and
311 homogeneous F-actin solutions with known concentrations under the same microscope (Fig. S6c).
312 The estimated actin density in the dense network is ~50 μM. This means that actin filaments are
313 spaced ~110 nm apart on average (Supplementary Note). Considering that the diameter of actin
314 filaments is ~8 nm (Blanchoin et al. 2014), this estimated value would be sparse enough for cofilin
315 to penetrate into the network by diffusion. As expected, cofilin labeled with a small fluorescence dye
316 penetrated into the dense network (Fig. S6d). Indeed, the cofilin density was proportional to the actin
317 density in a wide range from sparse to dense networks, indicating that cofilin can freely diffuse into
318 the network even in dense conditions (Fig. S6e). Notably, cofilin was enriched near the top of actin
319 pillars. This may be because cofilin has a higher affinity to ADP-actin than ATP-actin (Carlier et al.
320 1997). Collectively, these results clarified that the actin network disassembly mediated by cofilin is
321 also regulated by the network density. However, in the case of tiny cofilin, not the steric hindrance,
322 but the network structure such as the branching frequency or the degree of network entanglement
323 might contribute to the density-dependent suppression of the network disassembly.

324 Finally, to investigate whether the resistance to the cofilin-mediated network disassembly in
325 the dense network is influenced by the network shapes, we illuminated the SLB with various patterns.
326 Interestingly, the assembled network gradually floated, presumably due to actin disassembly
327 preferentially from the network surface, and kept their shapes in any patterns for over 40 min (Fig.
328 5d, Movie S6). Moreover, the floating actin networks were repeatedly created from the same position
329 by on/off cycles of the illumination (Fig. 5e, Movie S7). These results indicate that the effect of cofilin

on the network disassembly is dependent on the network density but independent of the network shapes.

Discussion

In this study, we developed an optogenetic tool, OptoVCA, which enables us to manipulate the assembly of Arp2/3-mediated actin networks by illuminating blue light. The strategy is applicable for both mammalian culture cells and *in vitro* reconstitution systems composed of purified actin cytoskeletal proteins and the SLB. We showed that the OptoVCA system can precisely control the density, thickness, and shape of actin networks on the same SLB by changing the illumination powers, durations, and patterns, respectively. Several papers have reported the techniques to localize NPFs to specified areas on the SLB or the glass surface, and succeeded in forming the Arp2/3-mediated actin networks *in vitro* (Yamazaki et al. 2024; Colin et al. 2023; Boujemaa-Paterski et al. 2017; Bieling et al. 2016; Manhart et al. 2019; Anne-Cécile Reymann et al. 2010). However, the removal of NPFs from the substrate was technically limited, making it difficult to stop actin polymerization during the observation. Our optogenetic approach has overcome this limitation by simply stopping the illumination, enabling us to create the actin network with a desired thickness. Therefore, a thin actin structure such as the actin cortex can be reconstituted by our approach (Fig. 4e-k). More biologically relevant actin networks can also be reconstituted by combining other NPFs and crosslinker proteins with the OptoVCA. However, there are two remaining issues to be addressed in the OptoVCA system. First, in our current design, the excess SspB-mScarlet-I-VCA is diffusing in the bulk region so that actin polymerization in the bulk region cannot be completely suppressed. Bright aggregations frequently observed in the bulk region may be caused by such a mechanism and it may reduce the effective concentrations of the loaded proteins (Fig. 2c, 5d, 5e, S3c, S3e). Consistently, the overexpression of the SspB-mScarlet-I-VCA in mammalian cells enhanced cytoplasmic signals of the Lifeact-miRFP703 under dark conditions (Fig. 1b). Further improvement of the protein design, such as the light-induced formation of functional VCA domain through the dimerization of split V domain and CA domain, is needed to suppress the basal activity of the VCA domain. Second, in *in vitro* experiments, the leak of the recruited VCA domain from the illuminated regions by its lateral diffusion reduces the spatial resolution of the control of actin polymerization (Fig. 2b, 2i). Combining the spatially patterned SLB with the OptoVCA would solve this problem (Yamazaki et al. 2024).

Using the OptoVCA system, we examined whether myosin filaments and cofilin are excluded from the actin network depending on the network density (Fig. 4, 5). The maximum actin density in our experiments was estimated to be ~50 μM (Fig. S6c). The estimated density is relatively low compared to the F-actin concentration in lamellipodium ~500 μM (Pollard 2016; Abraham et al. 1999; Koestler et al. 2009). Here, if it is assumed that the area covered with a single lipid molecule is 0.64 nm^2 (König, Dietrich, and Klose 1997) and iLID is fully activated on the SLB, the maximum density of SspB-mScarlet-I-VCA on the 6% DGS-NTA(Ni) lipid is estimated to be ~90,000 molecules/μm^2.

366 This density is approximately three-fold higher than that measured in live cells (Arasada and Pollard
367 2011; Ditlev et al. 2012). Therefore, the possible reason for the relatively low actin network density
368 may not be because of the lower density of VCA on the SLB but because of the other factors, such
369 as lower concentrations of Arp2/3 and F-actin fragments and the lack of volume exclusion effects
370 from the cytoplasm. Even in such conditions, we observed that myosin filaments with the mean length
371 of 1.32 μm were excluded and trapped at the side surface of the network in which actin filaments are
372 spaced 110 nm apart on average (Fig. 4, S6c, Supplementary Note). On the other hand, under
373 conditions where the actin filament spacing is estimated to be 160 nm or larger, we observed the
374 localization of myosin filaments within the network (Fig. 4a, S6c, Supplementary Note). The
375 threshold spacing distance determining whether myosin filaments can penetrate into the network is
376 expected to be between 110 nm and 160 nm. This value is comparable to the minimum size of myosin
377 filaments used in the experiments (Fig. S5b). Thus, our *in vitro* experiments provided direct evidence
378 that the ability of myosin penetration into the actin network is strictly regulated by the network density.
379 Strikingly, we found that only a ~2.5-fold increase in the network density, in other words, only a
380 ~1.5-fold increase in the mean actin mesh size, drastically changed the ability of myosin penetration
381 (Fig. 4a, 4b, 4c). This strengthens the idea that the exclusion of myosin observed in the cellular actin
382 cortex is attributable to the steric hindrance effect (Truong Quang et al. 2021). Interestingly, the
383 myosin signal was undetectable at the top surface of the pillar, while a strong myosin signal was
384 detected at the side surface (Fig. S5c). This might be due to the difference in the orientation of actin
385 filaments between the side surface and the top surface of the pillar. On the side surface, actin filaments
386 form an organized structure in which filaments are partially aligned, allowing myosin filaments to
387 remain stably attached. On the top surface, actin filaments may form a disorganized spiky structure,
388 leading to rapid dissociation of bound myosin filaments (Fig. 6). This mechanism might also
389 contribute to the exclusion of myosin filaments from the actin cortex in mouse oocytes observed when
390 the overexpressed VCA domain was localized beneath the plasma membrane (Chaigne et al. 2015).
391 Moreover, in sparse conditions, we found that the motor activity enhances the penetration ability of
392 myosin filaments into the network (Fig. S5d, S5f). In this way, the penetration ability of myosin
393 filaments is regulated by the actin network density, orientation of actin filaments, and myosin motor
394 activity (Fig. 6).
395 In the case of cofilin, penetration was observed even in the densest condition (Fig. S6d). While
396 the cofilin density was proportional to the actin density (Fig. S6e), the efficiency of the network
397 disassembly was sharply decreased in the networks with the actin concentration above 20-30 μM.
398 Therefore, this density-dependent suppression of cofilin-mediated network disassembly cannot be
399 explained by the steric hindrance effect. To consider the possible mechanism, we estimate the
400 filament level structure of the actin network used in the experiments. First, the mean length of actin

401 filament branches in the dense condition is estimated to be ~1-2 μm (Supplementary Note) (Pollard
402 2016; Schafer, Jennings, and Cooper 1996; Wear et al. 2003). Next, the density of actin molecules in
403 the dense network is estimated to be ~30,000/μm^3. Therefore, the network is estimated to be
404 composed of 40-80 actin filament branches per 1 μm^3. There are two possibilities that can explain the
405 density-dependent suppression mechanism of cofilin-mediated network disassembly. One possibility
406 is that the severed actin fragments are less likely to escape from the dense network than from the
407 sparse network because of the network entanglement if it is assumed that the frequency of the actin
408 filaments severing by cofilin is the same between sparse and dense networks. Another possibility is
409 the conformational difference in actin filaments between sparse and dense networks. The cofilin-
410 mediated severing of actin filaments is known to be dependent on the twisting of actin (McGough et
411 al. 1997). In dense networks, the higher frequency of Arp2/3-mediated branching of actin filaments
412 and/or the entanglement with surrounding filaments may impair the twisting, potentially reducing the
413 probability of cofilin-mediated severing of actin filaments. To further explore the network density-
414 dependent effect of cofilin, it will be important to investigate the impact of ABPs on the severing
415 activity of cofilin in single actin filament level and the diffusivity of F-actin fragments in the branched
416 actin network.

417 We showed that the actin sheet flowed toward the denser network in the presence of myosin
418 filaments (Fig. 4g, 4k). On the other hand, the sparsest network was disconnected from the directed
419 flow (Fig. 4k). These observations clarified that controlling only two parameters, the network density
420 gradient and the network connectivity, are sufficient to induce the directed flow and control the flow
421 direction. In other words, our study clarified that the spatial regulation of myosin activity is not always
422 required to induce the directed flow. In living cells, actin flow contributes to the deformation
423 processes during migration, cytokinesis, and oogenesis (Munro, Nance, and Priess 2004; Wolke,
424 Jezuit, and Priess 2007; Kelkar, Bohec, and Charras 2020; Paluch, Aspalter, and Sixt 2016). Such
425 cellular deformability may be facilitated by regulating the spatial gradient of the actin network within
426 a density range that myosin filaments can penetrate and the network is connected (i.e. dense condition
427 with 0.05% output or sparse condition with 0.05-0.35% in Fig. 4a). In addition, as the actin flow
428 proceeds, we observed the fusion and alignment of the myosin signal (Fig. 4g, 4k). It has been
429 observed in mammalian cells that several myosin filaments stack into a single thick filament during
430 the constriction of the contractile rings (Fenix et al. 2016; Yamamoto et al. 2019; Nilay et al. 2020).
431 This stacked structure is considered to be important for the generation of sufficient contractile force
432 (Fenix et al. 2016). The formation of the contractile ring is a sequential process that follows cortical
433 flow from the poles to the equator within the actin cortex (Anne-Cecile Reymann et al. 2016; Bray
434 and White 1988). The actin flow and myosin alignments observed in our study resemble this

435 sequential process. Therefore, our study may highlight the importance of the density gradient of the
436 actin network in the contractile ring formation process.

437 In summary, the OptoVCA system provides us with a flexible platform to reconstruct
438 branched actin networks with various densities, thicknesses, and shapes. Taking these advantages,
439 we provide direct evidence that the penetration ability of ABPs and their functions are tightly
440 regulated by the actin network density. Moreover, by creating the actin sheet that has the density
441 gradient, we identified the minimum factors sufficient to induce the directed actin flow. The actin
442 network is broadly distributed throughout the cell with various densities, including the cortex,
443 lamellipodia, and cytoplasm. Moreover, recent studies have increasingly suggested that the actin
444 network regulates the distribution of organelles (Moore et al. 2021; Olguin-Olguin et al. 2021).
445 Therefore, exploring the relationship between the network densities and protein or organelle sizes
446 using an *in vitro* reconstitution system may help to understand not only the cell mechanics but also
447 the compartmentalization mechanism within the cell in the future.

448 # Methods

449 **Plasmids**

450 The oligonucleotides for PCR and DNA sequencing were purchased from Eurofin. The cDNAs of
451 WAVE1 and cofilin were cloned from cDNA synthesized from mouse total RNA (Clontech).
452 pCAGGS-Stargazin-mEGFP-iLID and pCAGGS-SspB-mScarlet-I were purchased from Addgene
453 (#178523 and #178521, respectively). To construct pCAGGS-SspB-mScarlet-I-VCA, the VCA
454 domain sequence of WAVE1 was inserted into pCAGGS-SspB-mScarlet-I using Gibson assembly
455 cloning. For pET-28a(+)-His-mEGFP-iLID, the cDNAs of mEGFP and iLID were codon optimized
456 for *E.coli,* synthesized (Eurofin), and inserted into the pET-28a(+) vector using Gibson assembly
457 cloning. For pGEX-6P-1-SspB-mScarlet-I-VCA, the cDNAs of SspB and mScarlet-I were codon
458 optimized for *E.coli* and synthesized (Eurofin), and inserted into the pGEX-6P-1 vector using Gibson
459 assembly cloning. After that, the VCA domain sequence was amplified from pCAGGS-SspB-
460 mScarlet-I-VCA and subsequently inserted into the vector using Gibson assembly cloning. To
461 construct pRSET-mCofilin1, the cofilin sequence was inserted into the pRSET vector by Gibson
462 assembly cloning. pGEX-5X-hZIPK was a kind gift from Dr. Kozue Hamao (Hiroshima University).
463
464

465 **Protein expression and purification**

466 His-mEGFP-iLID

467 His-mEGFP-iLID was expressed in BL21 (DE3) in MMI medium. The cells were grown at 37°C
468 until the OD600 was reached at 0.6. The protein expression was induced by the addition of 1 mM
469 isopropyl-β-D-thiogalactopyranoside (IPTG). The cells were shaken at 160 rpm at 22°C for 20 hours.
470 The collected cells were resuspended in PBS (pH 7.4) containing 20 mM imidazole-HCl pH 7.4, 10
471 μg/mL leupeptin, 10 μg/mL pepstatin, 10 μg/mL chymostatin, and 1 mM PMSF. After sonication and
472 centrifugation, the supernatant was collected and loaded onto the HisTrap HP column (Cytiva), which
473 was controlled by AKTA Start (Cytiva). After the column washes with 500 mM NaCl containing 20
474 mM imidazole-HCl pH 7.4, the protein was eluted with 500 mM NaCl containing 500 mM imidazole-
475 HCl pH 7.4. The eluted protein fractions were concentrated using Amicon Ultra-4 (30 K MWCO,
476 Millipore) and gel-filtrated over the Superdex 200 Increase 10/300 GL column with A50 buffer (50
477 mM HEPES-KOH pH7.6, 50 mM KCl, 5 mM $MgCl_2$, 1 mM EGTA) containing 1 mM DTT,
478 controlled by the AKTA Explorer. Finally, the protein was snap-frozen in liquid nitrogen and stored
479 at –80°C.
480

481 SspB-mScarlet-I-VCA

482 SspB-mScarlet-I-VCA was expressed in BL21 (DE3) in MMI medium. The cells were grown at 37 °C
483 until the OD600 was reached at 0.6. The expression was induced by the addition of 1 mM isopropyl-
484 β-D-thiogalactopyranoside (IPTG). The cells were shaken at 160 rpm at 22 °C for 20 hours. The
485 collected cells were resuspended in PBS (pH 7.4) containing 10 μg/mL leupeptin, 10 μg/mL pepstatin,
486 10 μg/mL chymostatin, and 1 mM PMSF. After sonication and centrifugation, the supernatant was
487 collected and loaded onto the GSTrap HP column (Cytiva). After the column wash with PBS and 5
488 volumes of PreScission cleavage buffer (50 mM Tris-HCl pH7.5, 150 mM NaCl, 1 mM EDTA, 1
489 mM DTT), PreScission Protease (Cytiva) was injected into the column. Then, the column was
490 incubated at 4 °C overnight to remove GST-tag. The cleaved protein was collected and gel-filtrated
491 over the Superdex 200 Increase 10/300 GL column with A50 buffer containing 1 mM DTT, controlled
492 by the AKTA Explorer. Finally, the protein was snap-frozen in liquid nitrogen and stored at –80 °C.
493
494 Actin
495 Actin was purified from the acetone-dried powder of rabbit skeletal muscle (M6890, Sigma)
496 according to a previous report (Spudich and Watt 1971). The purified actin was labeled with Alexa
497 Fluor 647 C5 Maleimide (Invitrogen). Labeled actin was clarified by gel-filtration over Superdex 200
498 Increase 10/300 GL column (Cytiva) in G-buffer (2 mM Tis-HCl pH8.0, 0.05 mM $CaCl_2$, 2 mM
499 NaN_3, 0.1 mM ATP, 0.5 mM 2-mercaptoethanol). Both unlabeled and labeled actin in G-buffer were
500 snap -frozen in liquid nitrogen and stored at –80 °C.
501
502 Cofilin
503 Cofilin was expressed in BL21 (DE3) in MMI medium. The cells were grown at 37 °C until the
504 OD600 was reached at 1.0. The expression was induced by the addition of 1 mM IPTG. The cells
505 were shaken with 130 rpm at 25 °C for 3 hours. The collected cells were resuspended in PBS (pH
506 7.4) containing 10 μg/mL leupeptin, 10 μg/mL pepstatin, 10 μg/mL chymostatin, and 1 mM PMSF.
507 After sonication and centrifugation, the supernatant was collected and loaded onto the GSTrap HP
508 column (Cytiva). After the column wash with PBS and 5 volumes of PreScission cleavage buffer,
509 PreScission Protease (Cytiva) was injected into the column. Then, the column was incubated at 4 °C
510 overnight to remove GST-tag. The cleaved protein was collected and concentrated using Amicon
511 Ultra-4 (3 K MWCO, Millipore), and then gel-filtrated over the Superdex 200 Increase 10/300 GL
512 column with A50 buffer containing 1 mM DTT, controlled by the AKTA Explorer. For fluorescence
513 labeling, the protein was mixed with Alexa Fluor 546 NHS Ester (Invitrogen), and incubated at 4 °C
514 overnight. The reaction was stopped by adding 10 mM Tris-HCl (pH 7.5) and the protein was gel
515 filtrated at the same condition as the non-labeled protein. Both unlabeled and labeled cofilin were
516 snap-frozen in liquid nitrogen and stored at –80 °C.

517

518 Myosin

519 Unphosphorylated smooth muscle myosin (SMM) was purified from chicken gizzards as previously
520 reported (Ikebe and Hartshorne 1985). The extracted sample was further dialyzed at 4°C overnight,
521 against A50 buffer containing 1 mM DTT and 0.5 mM ATP. After the addition of 0.5 mM fresh ATP
522 to the dialyzed sample, it was centrifuged at 20,000 x g for 10 min at 4°C to remove aggregates and
523 contaminating phosphorylated myosin. The purified protein was labeled with Alexa Fluor 546 NHS
524 Ester (Invitrogen), snap-frozen in liquid nitrogen, and stored at –80°C.

525

526 ZIP kinase

527 Recombinant human ZIPK was prepared according to a previous report with slight modifications
528 (Kondo et al. 2012). Briefly, the protein was expressed in *E. coli* (Rosetta 2 (DE3), Merck Millipore)
529 at 25°C for 1 h in the presence of 1 mM IPTG. The GST-tagged proteins were purified using a
530 glutathione Sepharose column (GSTrap HP, GE Healthcare), followed by overnight dialysis against
531 A50 buffer containing 1 mM DTT at 4°C. Samples were centrifuged at 627,000 x g for 20 min at 4°C
532 to remove aggregates, snap-frozen in liquid nitrogen, and stored at –80°C.

533

534 Arp2/3

535 The Arp2/3 complex was purchased from Cytoskeleton Inc. The protein was diluted with a buffer
536 containing 20 mM Tris-HCl (pH 7.5), 25 mM KCl, 1 mM $MgCl_2$, 0.5 mM EDTA, 0.1 mM ATP, and
537 1 mM DTT. The protein was snap-frozen with liquid nitrogen and stored at –80°C.

538

539 Profilin

540 Profilin was purified according to our previous report (Kubota et al. 2017).

541

542 Capping protein

543 Capping protein was purified according to our previous report (Yamazaki et al. 2024).

544

545

546 **Cell culture and live imaging**

547 MDCK cells (no. RCB0995: RIKEN Bioresource Center) stably expressing Lifeact-miRFP703 were
548 a kind gift from Dr. Kazuhiro Aoki (Kyoto University). The cells were maintained in DMEM (08459-
549 64, Nacalai Tesque) supplemented with 10% fetal bovine serum (FBS; F7524-500ML, Sigma), 100
550 units/mL penicillin and 100 μg/mL streptomycin (168-23191, Wako) in a 5% CO_2 humidified
551 incubator at 37°C. For the passage of the MDCK cells, the growth media was removed, and the cells

552 were washed with 3 mL PBS. Next, 3 mL PBS containing 1 mM EDTA and 0.25% trypsin (18172-
553 94: Nacalai Tesque) was added, immediately removed and the cells were incubated for 5 min at 37 °C.
554 Prewarmed DMEM was added to resuspend the cells.
555 To observe the trypsinized cells, the cells were detached from the 6-well plates under dark
556 conditions. Next, the cells were suspended with 200 μL FluoroBrite (A1896702, Gibco)
557 supplemented with 10% FBS, 100 units/mL penicillin, and 100 μg/mL streptomycin, and plated on
558 the collagen-coated 35 mm glass-bottom dishes. The imaging was started within 10 min after the
559 seeding. During live-cell imaging, cells were incubated with a stage incubator set to 37 °C and
560 containing 5% CO_2 (STXG-IX3WX; Tokai Hit). The 488 nm laser was globally illuminated from the
561 objective lens for the activation of iLID.
562
563
564 **Transfection**
565 Since the VCA domain of WAVE1 fused with fluorescence protein tends to aggregate for long-term
566 expression, all of the experiments were performed by transient expression. The MDCK cells were
567 electroporated by using a 4D-Nucleofector (Lonza) according to the manufacturer's instructions
568 (CA152 program) and attached solutions. For transient expression, 10 μg of total plasmids were
569 mixed with the mass ratio of SspB:iLID = 1:4 to achieve efficient membrane translocation by light.
570 After electroporation, the cells were incubated at room temperature for 10 min and plated on the 6-
571 well culture plates (VTC-T6, AS ONE) or collagen-coated 35-mm glass-base dishes (D11130H,
572 Matsunami). The cells were imaged 18-24 hours after the electroporation.
573
574
575 **Drug treatment**
576 An Arp2/3 inhibitor, CK-666 (SML0006, Sigma-Aldrich), was diluted with DMSO (D2650, Sigma-
577 Aldrich) at a concentration of 50 mM. The CK-666 treatment at a final concentration of 50 μM started
578 30 min before trypsinization. The concentration was maintained during live-cell imaging. A myosin
579 II ATPase inhibitor, blebbistatin (B0560, Sigma-Aldrich), was diluted with DMSO (D2650, Sigma-
580 Aldrich) at a concentration of 10 mM. The assembled SMM filaments were treated with blebbistatin
581 at a final concentration of 50 μM 10 min before mixing with other proteins. The concentration was
582 maintained during imaging. Although blebbistatin has been reported to be inactivated by blue light,
583 the measured illumination intensity was at least 100-fold weaker than the intensity which can not be
584 inactivated (Fig. S4a, S4b) (Sakamoto et al. 2005).
585
586

587 **Confocal microscopy**

588 An inverted microscope (ECLIPSE Ti2, Nikon) equipped with an EMCCD camera (iXon Life 888,
589 ANDOR), a spinning disk confocal unit (CSU-W1, Yokogawa Electric Corporation), and an oil
590 immersion objective lens (CFI Plan Lambda D 60x, N.A. 1.42, Nikon) was used. The excitation laser
591 and fluorescence filter settings were as follows: Excitation laser, 405 nm, 488 nm, 561 nm, and 640
592 nm; dichroic mirror, DM 405/488/568/647; emission filters, 447/60 nm, 525/50 nm, 617/73 nm, and
593 685/40 nm. The microscope was controlled by NIS-elements software (Ver. 5.42.03, Nikon). For
594 global light illumination, 500 msec of pulsed blue light (488 nm) was illuminated through the
595 objective lens with 20 sec intervals. For local light illumination, a digital micromirror device module
596 (Nikon) and a light source SOLA (Lumencor) were mounted on the ECLIPSE Ti2 system and 500
597 msec of pulsed blue light was illuminated through the objective lens with 20 sec intervals. The filter
598 settings for the digital micromirror device were as follows: Dichroic filter, 500; excitation filter
599 470/40 nm; emission filter, 535/50 (GFP-B, Nikon). To reduce the light intensity, an ND filter
600 (NE220B, Thorlabs) was inserted into the light path of the SOLA. The light intensity irradiated by
601 the digital micromirror device was measured by a power meter (TQ8210, Advantest). Briefly, the
602 sensor panel was attached to the objective lens, then blue light was illuminated and intensity was
603 recorded with various light intensities and illumination patterns.
604
605
606 **TIRF microscopy**

607 Single-molecule imaging was performed using hand-made TIRF microscopy. An inverted
608 microscope (IX73, Olympus) equipped with an EMCCD camera (iXon3, Andor), the excitation laser
609 (OBIS 488 nm LS, Coherent), and an oil immersion objective lens (PlanApo 60x, N.A. 1.45, TIRFM,
610 Olympus) were used.
611
612
613 **Preparation of the lipid bilayer**

614 1-palmitoyl-2-oleoyl-sn-glycero-3-phosphocholine (POPC) and 1,2-dioleoyl-sn-glycero-3-[(N-(5-
615 amino-1-carboxypentyl)iminodiacetic acid)succinyl] (nickel salt) (DGS-NTA(Ni)) were purchased
616 from Avanti Polar Lipids. 1,2-Dihexadecanoyl-sn-Glycero-3-Phosphoethanolamine (Marina Blue
617 DHPE) was purchased from Invitrogen. Each lipid was dissolved in chloroform within a round-
618 bottom glass tube at a concentration of 20 mM. Next, DGS-NTA(Ni) was mixed with POPC at 2
619 mol% or 6 mol% in a new glass tube. To visualize the lipid, Marina Blue DHPE was also mixed at 2
620 mol% as needed. The lipids were dried by vacuuming overnight. The lipid-dried film was then
621 hydrated with PBS (pH 6.5) overnight. The final lipid concentration was adjusted to 1 mM. The

622 hydrated lipids were dispersed by five freeze-thaw cycles using liquid nitrogen and hot water at 30 °C.
623 The lipids were stored at –30 °C and used within two months.
624 Functionalized coverslips were prepared as follows. First, coverslips (Matsunami, 24 × 60
625 mm, thickness No.1, non-coating) were sonicated in a mixture of 80% Ethanol and 5% NaOH for 90
626 min. Then, the coverslips were washed with Milli-Q water 5 times and sonicated again in Milli-Q
627 water for 30 min. Finally, the coverslips were washed with Milli-Q water 5 times and stored in Milli-
628 Q water at room temperature. The coverslips were used within 2 weeks. We then made a hand-made
629 flow cell by putting double-sided tapes and then putting an 18 × 18 mm non-treated coverslip
630 (Matsunami) on the functionalized coverslip. Before use, the functionalized coverslip was dried with
631 a nitrogen gas stream and cleaned in the plasma cleaner (PDC-32G: Harrick Plasma) for 5 min. The
632 volume of the flow cell was about 10 μL. The lipid solution was diluted 4 times with PBS (pH 6.5),
633 filtrated using a Mini-Extruder Set (610000: Avanti Polar Lipids), and loaded into the flow cell. The
634 flow cells were incubated for 10 min to make a lipid bilayer by vesicle fusion. Unfused vesicles were
635 removed by washing with 50 μL of Milli-Q water.
636
637
638 **Preparation of the actin polymerization solution**
639 All the following procedures were conducted at room temperature under red light to avoid activating
640 iLID. First, 50 μL of His-mEGFP-iLID at a concentration of 7 μM was loaded into the flow cell.
641 After 5 min incubation, unbound His-mEGFP-iLID was removed by washing with 50 μL of A50
642 buffer. Immediately after the washing, the actin polymerization solution was loaded into the flow cell,
643 and the periphery of the flow cell was sealed with VaLaP. Then, the flow cell was mounted on the
644 microscope and the imaging was started within 2 min.
645 During 5 min incubation of His-mEGFP-iLID, the actin polymerization solution was prepared.
646 The total volume of the mixture was 20 μL in A50 buffer and the final composition was 2 mM Trolox,
647 10 μM FMN (F8399, Sigma-Aldrich), energy mix (1 mM ATP, 10 mM phosphocreatine, 0.1 mg/mL
648 creatine phosphokinase, 10 mM DTT in A50 buffer), profilin, actin (10 mol % labeled with Alexa647),
649 capping protein, Arp2/3, and SspB-mScarlet-I-VCA. Note that actin was incubated on ice for more
650 than 10 days after thawing and then used within 2 months. SMM and cofilin were also added to the
651 solution, as needed. Although SMM and cofilin were detected by the same image channel as the
652 SspB-mScarlet-I-VCA, it was easy to distinguish these proteins from SspB-mScarlet-I-VCA because
653 of their distinct distributions. The concentrations of each protein are noted in each figure legend. To
654 phosphorylate SMM, 1 μM SMM (40 mol % labeled with Alexa546), 100 nM ZIP kinase, and energy
655 mix were mixed and incubated at 25 °C for 90 min. The SMM solution was used within 2 days.
656

657

658 **Pyrene actin polymerization assay**

659 To measure the actin polymerization activity by pyrene fluorescence, 20 μM Actin (5 mol % labeled
660 with pyrene) in a G-buffer was kept on ice more than 3 days before the measurement. First, 20 μL of
661 20 μM Actin was loaded into 6-wells of a 384-well plate. Next, 60 μL of 4/3× A50 buffer containing
662 4/3× energy mix and ABPs was loaded. The final concentrations were 2 mM Trolox, 10 μM FMN,
663 15 μM profilin, 25 nM capping protein, 50 nM Arp2/3, 7 μM His-mEGFP-iLID, and 1 μM SspB-
664 mScarlet-I-VCA. The fluorescence intensities of pyrene for each condition were simultaneously
665 measured using a fluorescence plate reader (FluoroskanFL, Thermo Fisher Scientific) at 25°C for 20
666 min at 15 sec intervals. The minimum value for each condition was defined as the background noise
667 and subtracted from each time-series data point.

668

669

670 **Measurement of SMM filament length**

671 To induce SMM filament formation, 1 μM SMM (40 mol % labeled with Alexa546) was incubated
672 with 100 nM ZIP kinase, energy mix in A50 buffer at 25 °C for 90 min. Then, the sample was diluted
673 100 times with A50 buffer containing 1 mM ATP and 10 mM DTT. The diluted sample was observed
674 under confocal microscopy (see "confocal microscopy"). An oil immersion objective lens (CFI Plan
675 Lambda D 100 x, N.A. 1.45; Nikon) was used. After background subtraction, the FWHM value along
676 the short axis of SMM filaments was used to determine the threshold and then the raw images were
677 binarised. The length of the long axis of each filament was measured as the filament length. The
678 overlapping filaments were manually excluded from the analysis.

679

680

681 **Imaging analysis**

682 Fluorescence imaging data were analyzed and quantified using Fiji (Image J). The fluorescence
683 images were quantified after subtracting the background using the rolling ball function in Fiji unless
684 otherwise described. The quantified data was plotted using Python. Three-dimensional images were
685 reconstructed by the depth-coded alpha blending function of NIS-elements software (Nikon). To
686 quantify the cortical fluorescence intensity of MDCK cells, we used a custom-made Fiji macro (Fig.
687 1c, 1d, 1g, S1b, S1c, S1e). Briefly, after the subtraction of the background, the images of Lifeact-
688 miRFP703 were binarized. Next, to smooth the cell periphery, the images were enlarged twice and
689 shrunk twice using dilate and erode functions in Fiji, respectively, and added as the first ROI. The
690 first ROI was shrunk by 4 pixels and added as the second ROI. Finally, the area between the first and
691 the second ROIs was analyzed as the cortical region, and the internal area of the second ROI was

692 analyzed as the cytoplasmic region. To quantify the fluorescence intensity on the SLB, a single z-
693 slice nearest to the coverslip surface was measured unless otherwise described. To measure the actin
694 pillar length, the z-axis images were reconstructed by NIS-elements software (Fig. 2h, S4c). The
695 distance from z = 0 μm to the center of the pillar was manually measured. To show the actin flow,
696 the function of maximum intensity projection in Fiji was used (Fig. 4d, 4f, 4g, 4k). The temporal
697 color-coded image of the actin flow was created after filling the floating protein aggregations with
698 black color (Fig. 4h). To quantify the fluorescence intensity of Alexa647-actin in the presence of
699 cofilin (Fig. 5b, S6a, S6b), the maximum intensity projection images were used because the actin
700 pillars were detached from the SLB after stopping illumination. To quantify the actin disassembly
701 level, the fluorescence intensities of actin 10 min after stopping illumination were divided by the
702 fluorescence intensities of actin 10 min after starting illumination (the last frame before stopping
703 illumination) in each pillar (Fig. 5c). The samples not showing visible actin polymerization were
704 excluded from the scatter plots. The power-law fitting was performed using data with the actin
705 fluorescence greater than 0.3 to eliminate the influence of the background signal.
706
707
708 **Statistics and reproducibility**
709 In all box-and-whisker plots, the box shows the quartiles of data with the whiskers denoting the
710 minimum and maximum except for the outliers detected by 1.5 times the interquartile range. The
711 statistical analysis was performed by Python. The experiments were repeated at least twice
712 independently, to confirm reproducibility. The sample number for quantification is listed in the figure
713 legends.

714 **References**

715 Abraham, Vivek C., Vijaykumar Krishnamurthi, D. Lansing Taylor, and Frederick Lanni. 1999.
716 "The Actin-Based Nanomachine at the Leading Edge of Migrating Cells." *Biophysical Journal*
717 77 (3): 1721–32.
718 Alekhina, Olga, Ezra Burstein, and Daniel D. Billadeau. 2017. "Cellular Functions of WASP
719 Family Proteins at a Glance." *Journal of Cell Science* 130 (14): 2235–41.
720 Arasada, Rajesh, and Thomas D. Pollard. 2011. "Distinct Roles for F-BAR Proteins Cdc15p and
721 Bzz1p in Actin Polymerization at Sites of Endocytosis in Fission Yeast." *Current Biology: CB*
722 21 (17): 1450–59.
723 Berlew, Erin E., Keisuke Yamada, Ivan A. Kuznetsov, Eleanor A. Rand, Chandler C. Ochs, Zaynab
724 Jaber, Kevin H. Gardner, and Brian Y. Chow. 2022. "Designing Single-Component
725 Optogenetic Membrane Recruitment Systems: The Rho-Family GTPase Signaling Toolbox."
726 *ACS Synthetic Biology* 11 (1): 515–521.
727 Bieling, Peter, Tai-De Li, Julian Weichsel, Ryan McGorty, Pamela Jreij, Bo Huang, Daniel A.
728 Fletcher, and R. Dyche Mullins. 2016. "Force Feedback Controls Motor Activity and
729 Mechanical Properties of Self-Assembling Branched Actin Networks." *Cell* 164 (1-2): 115–27.
730 Blanchoin, Laurent, Rajaa Boujemaa-Paterski, Cécile Sykes, and Julie Plastino. 2014. "Actin
731 Dynamics, Architecture, and Mechanics in Cell Motility." *Physiological Reviews* 94 (1): 235–
732 63.
733 Boujemaa-Paterski, Rajaa, Cristian Suarez, Tobias Klar, Jie Zhu, Christophe Guérin, Alex
734 Mogilner, Manuel Théry, and Laurent Blanchoin. 2017. "Network Heterogeneity Regulates
735 Steering in Actin-Based Motility." *Nature Communications* 8 (1): 655.
736 Bravo-Cordero, Jose Javier, Marco A. O. Magalhaes, Robert J. Eddy, Louis Hodgson, and John
737 Condeelis. 2013. "Functions of Cofilin in Cell Locomotion and Invasion." *Nature Reviews.*
738 *Molecular Cell Biology* 14 (7): 405–15.
739 Bray, D., and J. G. White. 1988. "Cortical Flow in Animal Cells." *Science (New York, N.Y.)* 239
740 (4842): 883–88.
741 Breitsprecher, Dennis, and Bruce L. Goode. 2013. "Formins at a Glance." *Journal of Cell Science*
742 126 (1): 1–7.
743 Carlier, M. F., V. Laurent, J. Santolini, R. Melki, D. Didry, G. X. Xia, Y. Hong, N. H. Chua, and D.
744 Pantaloni. 1997. "Actin Depolymerizing Factor (ADF/cofilin) Enhances the Rate of Filament
745 Turnover: Implication in Actin-Based Motility." *The Journal of Cell Biology* 136 (6): 1307–22.
746 Chaigne, A., C. Campillo, N. S. Gov, R. Voituriez, C. Sykes, M. H. Verlhac, and M. E. Terret.
747 2015. "A Narrow Window of Cortical Tension Guides Asymmetric Spindle Positioning in the

748 Mouse Oocyte." *Nature Communications* 6 (1):6027.
749 Chugh, Priyamvada, Andrew G. Clark, Matthew B. Smith, Davide A. D. Cassani, Kai Dierkes,
750 Anan Ragab, Philippe P. Roux, Guillaume Charras, Guillaume Salbreux, and Ewa K. Paluch.
751 2017. "Actin Cortex Architecture Regulates Cell Surface Tension." *Nature Cell Biology* 19 (6):
752 689–97.
753 Clarke, D. Nathaniel, and Adam C. Martin. 2021. "Actin-Based Force Generation and Cell
754 Adhesion in Tissue Morphogenesis." *Current Biology: CB* 31 (10): R667–80.
755 Colin, Alexandra, Magali Orhant-Prioux, Christophe Guérin, Mariya Savinov, Wenxiang Cao,
756 Benoit Vianay, Ilaria Scarfone, et al. 2023. "Friction Patterns Guide Actin Network
757 Contraction." *Proceedings of the National Academy of Sciences of the United States of*
758 *America* 120 (39): e2300416120.
759 Craig, Roger, and John L. Woodhead. 2006. "Structure and Function of Myosin Filaments."
760 *Current Opinion in Structural Biology* 16 (2): 204–12.
761 Derivery, Emmanuel, and Alexis Gautreau. 2010. "Generation of Branched Actin Networks:
762 Assembly and Regulation of the N-WASP and WAVE Molecular Machines." *BioEssays: News*
763 *and Reviews in Molecular, Cellular and Developmental Biology* 32 (2): 119–31.
764 Dimchev, Georgi, Anika Steffen, Frieda Kage, Vanessa Dimchev, Julien Pernier, Marie-France
765 Carlier, and Klemens Rottner. 2017. "Efficiency of Lamellipodia Protrusion Is Determined by
766 the Extent of Cytosolic Actin Assembly." *Molecular Biology of the Cell* 28 (10): 1311–25.
767 Ditlev, Jonathon A., Paul J. Michalski, Greg Huber, Gonzalo M. Rivera, William A. Mohler, Leslie
768 M. Loew, and Bruce J. Mayer. 2012. "Stoichiometry of Nck-Dependent Actin Polymerization
769 in Living Cells." *The Journal of Cell Biology* 197 (5): 643–58.
770 Dürre, Katharina, Felix C. Keber, Philip Bleicher, Fridtjof Brauns, Christian J. Cyron, Jan Faix, and
771 Andreas R. Bausch. 2018. "Capping Protein-Controlled Actin Polymerization Shapes Lipid
772 Membranes." *Nature Communications* 9 (1): 1630.
773 Espinoza-Sanchez, Sofia, Lauren Ann Metskas, Steven Z. Chou, Elizabeth Rhoades, and Thomas
774 D. Pollard. 2018. "Conformational Changes in Arp2/3 Complex Induced by ATP, WASp-
775 VCA, and Actin Filaments." *Proceedings of the National Academy of Sciences of the United*
776 *States of America* 115 (37): E8642–51.
777 Fenix, A. M., N. Taneja, C. A. Buttler, J. Lewis, S. B. Van Engelenburg, R. Ohi, and D. T.
778 Burnette. 2016. "Expansion and Concatenation of Nonmuscle Myosin IIA Filaments Drive
779 Cellular Contractile System Formation during Interphase and Mitosis." *Molecular Biology of*
780 *the Cell* 27 (9): 1465–78.
781 Firat-Karalar, Elif Nur, and Matthew D. Welch. 2011. "New Mechanisms and Functions of Actin
782 Nucleation." *Current Opinion in Cell Biology* 23 (1): 4–13.

García-Arcos, Juan Manuel, Ankita Jha, Clare M. Waterman, and Matthieu Piel. 2024. "Blebology: Principles of Bleb-Based Migration." *Trends in Cell Biology* 34 (10): 838–853.

Gautreau, Alexis M., Fred E. Fregoso, Gleb Simanov, and Roberto Dominguez. 2022. "Nucleation, Stabilization, and Disassembly of Branched Actin Networks." *Trends in Cell Biology* 32 (5): 421–32.

Guntas, Gurkan, Ryan A. Hallett, Seth P. Zimmerman, Tishan Williams, Hayretin Yumerefendi, James E. Bear, and Brian Kuhlman. 2015. "Engineering an Improved Light-Induced Dimer (iLID) for Controlling the Localization and Activity of Signaling Proteins." *Proceedings of the National Academy of Sciences of the United States of America* 112 (1): 112–17.

Huehn, Andrew R., Jeffrey P. Bibeau, Anthony C. Schramm, Wenxiang Cao, Enrique M. De La Cruz, and Charles V. Sindelar. 2020. "Structures of Cofilin-Induced Structural Changes Reveal Local and Asymmetric Perturbations of Actin Filaments." *Proceedings of the National Academy of Sciences of the United States of America* 117 (3): 1478–84.

Ikebe, M., and D. J. Hartshorne. 1985. "Effects of Ca2+ on the Conformation and Enzymatic Activity of Smooth Muscle Myosin." *The Journal of Biological Chemistry* 260 (24): 13146–53.

Jawahar, Anumita, Joseph Vermeil, Julien Heuvingh, Olivia du Roure, and Matthieu Piel. 2024. "The Third Dimension of the Actin Cortex." *Current Opinion in Cell Biology* 89: 102381.

Kadzik, Rachel S., Kaitlin E. Homa, and David R. Kovar. 2020. "F-Actin Cytoskeleton Network Self-Organization through Competition and Cooperation." *Annual Review of Cell and Developmental Biology* 36 (1): 35–60.

Kelkar, Manasi, Pierre Bohec, and Guillaume Charras. 2020. "Mechanics of the Cellular Actin Cortex: From Signalling to Shape Change." *Current Opinion in Cell Biology* 66 (June):69–78.

Koestler, Stefan A., Klemens Rottner, Frank Lai, Jennifer Block, Marlene Vinzenz, and J. Victor Small. 2009. "F- and G-Actin Concentrations in Lamellipodia of Moving Cells." *PloS One* 4 (3): e4810.

Komatsu, Satoshi, and Mitsuo Ikebe. 2004. "ZIP Kinase Is Responsible for the Phosphorylation of Myosin II and Necessary for Cell Motility in Mammalian Fibroblasts." *The Journal of Cell Biology* 165 (2): 243–54.

Kondo, Tomo, Rieko Isoda, Takashi Uchimura, Mutsumi Sugiyama, Kozue Hamao, and Hiroshi Hosoya. 2012. "Diphosphorylated but Not Monophosphorylated Myosin II Regulatory Light Chain Localizes to the Midzone without Its Heavy Chain during Cytokinesis." *Biochemical and Biophysical Research Communications* 417 (2): 686–91.

König, B., U. Dietrich, and G. Klose. 1997. "Hydration and Structural Properties of Mixed Lipid/surfactant Model Membranes." *Langmuir: The ACS Journal of Surfaces and Colloids* 13 (3): 525–32.

818 Kruse, Karsten, Rémi Berthoz, Luca Barberi, Anne-Cécile Reymann, and Daniel Riveline. 2024.
819 "Actomyosin Clusters as Active Units Shaping Living Matter." *Current Biology: CB* 34 (20):
820 R1045–58.
821 Kubota, Hiroaki, Makito Miyazaki, Taisaku Ogawa, Togo Shimozawa, Kazuhiko Kinosita Jr, and
822 Shin 'ichi Ishiwata. 2017. "Biphasic Effect of Profilin Impacts the Formin mDia1 Force-
823 Sensing Mechanism in Actin Polymerization." *Biophysical Journal* 113 (2): 461–71.
824 Kurisu, Shusaku, and Tadaomi Takenawa. 2009. "The WASP and WAVE Family Proteins."
825 *Genome Biology* 10 (6): 226.
826 Laplaud, Valentin, Nicolas Levernier, Judith Pineau, Mabel San Roman, Lucie Barbier, Pablo J.
827 Sáez, Ana-Maria Lennon-Duménil, et al. 2021. "Pinching the Cortex of Live Cells Reveals
828 Thickness Instabilities Caused by Myosin II Motors." *Science Advances* 7 (27): eabe3640.
829 Le Clainche, Christophe, Dominique Pantaloni, and Marie-France Carlier. 2003. "ATP Hydrolysis
830 on Actin-Related Protein 2/3 Complex Causes Debranching of Dendritic Actin Arrays."
831 *Proceedings of the National Academy of Sciences of the United States of America* 100 (11):
832 6337–42.
833 Manhart, Angelika, Téa Aleksandra Icheva, Christophe Guerin, Tobbias Klar, Rajaa Boujemaa-
834 Paterski, Manuel Thery, Laurent Blanchoin, and Alex Mogilner. 2019. "Quantitative
835 Regulation of the Dynamic Steady State of Actin Networks." *eLife* 8: e42413
836 McGough, A., B. Pope, W. Chiu, and A. Weeds. 1997. "Cofilin Changes the Twist of F-Actin:
837 Implications for Actin Filament Dynamics and Cellular Function." *The Journal of Cell Biology*
838 138 (4): 771–81.
839 Moore, Andrew S., Stephen M. Coscia, Cory L. Simpson, Fabian E. Ortega, Eric C. Wait, John M.
840 Heddleston, Jeffrey J. Nirschl, et al. 2021. "Actin Cables and Comet Tails Organize
841 Mitochondrial Networks in Mitosis." *Nature* 591(7851): 659–664.
842 Munro, Edwin, Jeremy Nance, and James R. Priess. 2004. "Cortical Flows Powered by
843 Asymmetrical Contraction Transport PAR Proteins to Establish and Maintain Anterior-
844 Posterior Polarity in the Early C. Elegans Embryo." *Developmental Cell* 7 (3): 413–24.
845 Murata-Hori, M., F. Suizu, T. Iwasaki, A. Kikuchi, and H. Hosoya. 1999. "ZIP Kinase Identified as
846 a Novel Myosin Regulatory Light Chain Kinase in HeLa Cells." *FEBS Letters* 451 (1): 81–84.
847 Nakamura, Hideki, Elmer Rho, Christopher T. Lee, Kie Itoh, Daqi Deng, Satoshi Watanabe, Shiva
848 Razavi, et al. 2023. "ActuAtor, a Listeria-Inspired Molecular Tool for Physical Manipulation
849 of Intracellular Organizations through de Novo Actin Polymerization." *Cell Reports* 42 (10):
850 113089.
851 Natwick, Dean E., and Sean R. Collins. 2021. "Optimized iLID Membrane Anchors for Local
852 Optogenetic Protein Recruitment." *ACS Synthetic Biology* 10 (5): 1009–1023.

853 Nilay, Matthew R., Sophie M. Bersi, Aidan M. Baillargeon, James A. Fenix, Ryoma Cooper,
854 Vivian Ohi, W. Gama, and Dylan T. David Merryman. 2020. "Precise Tuning of Cortical
855 Contractility Regulates Cell Shape during Cytokinesis." *Cell Reports* 31 (1): 107477.
856 Olguin-Olguin, Adan, Anne Aalto, Benoît Maugis, Aleix Boquet-Pujadas, Dennis Hoffmann, Laura
857 Ermlich, Timo Betz, Nir S. Gov, Michal Reichman-Fried, and Erez Raz. 2021. "Chemokine-
858 Biased Robust Self-Organizing Polarization of Migrating Cells in Vivo." *Proceedings of the*
859 *National Academy of Sciences of the United States of America* 118 (7): e2018480118
860 Paluch, Ewa K., Irene M. Aspalter, and Michael Sixt. 2016. "Focal Adhesion-Independent Cell
861 Migration." *Annual Review of Cell and Developmental Biology* 32 (October):469–90.
862 Pollard, Thomas D. 2016. "Actin and Actin-Binding Proteins." *Cold Spring Harbor Perspectives in*
863 *Biology* 8 (8): a018226.
864 Reymann, Anne-Cécile, Rajaa Boujemaa-Paterski, Jean-Louis Martiel, Christophe Guérin,
865 Wenxiang Cao, Harvey F. Chin, Enrique M. De La Cruz, Manuel Théry, and Laurent
866 Blanchoin. 2012. "Actin Network Architecture Can Determine Myosin Motor Activity."
867 *Science* 336 (6086): 1310–14.
868 Reymann, Anne-Cécile, Jean-Louis Martiel, Théo Cambier, Laurent Blanchoin, Rajaa Boujemaa-
869 Paterski, and Manuel Théry. 2010. "Nucleation Geometry Governs Ordered Actin Networks
870 Structures." *Nature Materials* 9 (10): 827–32.
871 Reymann, Anne-Cecile, Fabio Staniscia, Anna Erzberger, Guillaume Salbreux, and Stephan W.
872 Grill. 2016. "Cortical Flow Aligns Actin Filaments to Form a Furrow." *eLife* 5: e17807.
873 Sakamoto, Takeshi, John Limouze, Christian A. Combs, Aaron F. Straight, and James R. Sellers.
874 2005. "Blebbistatin, a Myosin II Inhibitor, Is Photoinactivated by Blue Light." *Biochemistry* 44
875 (2): 584–88.
876 Schafer, D. A., P. B. Jennings, and J. A. Cooper. 1996. "Dynamics of Capping Protein and Actin
877 Assembly in Vitro: Uncapping Barbed Ends by Polyphosphoinositides." *The Journal of Cell*
878 *Biology* 135 (1): 169–79.
879 Soares e Silva, Marina, Martin Depken, Björn Stuhrmann, Marijn Korsten, Fred C. MacKintosh,
880 and Gijsje H. Koenderink. 2011. "Active Multistage Coarsening of Actin Networks Driven by
881 Myosin Motors." *Proceedings of the National Academy of Sciences of the United States of*
882 *America* 108 (23): 9408–13.
883 Spudich, J. A., and S. Watt. 1971. "The Regulation of Rabbit Skeletal Muscle Contraction. I.
884 Biochemical Studies of the Interaction of the Tropomyosin-Troponin Complex with Actin and
885 the Proteolytic Fragments of Myosin." *The Journal of Biological Chemistry* 246 (15): 4866–71.
886 Straight, Aaron F., Amy Cheung, John Limouze, Irene Chen, Nick J. Westwood, James R. Sellers,
887 and Timothy J. Mitchison. 2003. "Dissecting Temporal and Spatial Control of Cytokinesis with

a Myosin II Inhibitor." *Science* 299 (5613): 1743–47.

Svitkina, Tatyana. 2018. "The Actin Cytoskeleton and Actin-Based Motility." *Cold Spring Harbor Perspectives in Biology* 10 (1): a018267.

Tanaka, Kotaro, Shuichi Takeda, Kaoru Mitsuoka, Toshiro Oda, Chieko Kimura-Sakiyama, Yuichiro Maéda, and Akihiro Narita. 2018. "Structural Basis for Cofilin Binding and Actin Filament Disassembly." *Nature Communications* 9: 1860.

Taslimi, Amir, Justin D. Vrana, Daniel Chen, Sofya Borinskaya, Bruce J. Mayer, Matthew J. Kennedy, and Chandra L. Tucker. 2014. "An Optimized Optogenetic Clustering Tool for Probing Protein Interaction and Function." *Nature Communications* 5: 4925.

Truong Quang, Binh An, Ruby Peters, Davide A. D. Cassani, Priyamvada Chugh, Andrew G. Clark, Meghan Agnew, Guillaume Charras, and Ewa K. Paluch. 2021. "Extent of Myosin Penetration within the Actin Cortex Regulates Cell Surface Mechanics." *Nature Communications* 12: 6511.

Vicente-Manzanares, M., X. Ma, R. S. Adelstein, and A. R. Horwitz. 2009. "Non-Muscle Myosin II Takes Centre Stage in Cell Adhesion and Migration." *Nature reviews.Molecular Cell Biology* 10 (11): 778–90.

Wear, Martin A., Atsuko Yamashita, Kyoungtae Kim, Yuichiro Maéda, and John A. Cooper. 2003. "How Capping Protein Binds the Barbed End of the Actin Filament." *Current Biology: CB* 13 (17): 1531–37.

Wolke, Uta, Erin A. Jezuit, and James R. Priess. 2007. "Actin-Dependent Cytoplasmic Streaming in C. Elegans Oogenesis." *Development (Cambridge, England)* 134 (12): 2227–36.

Yamamoto, Kei, Haruko Miura, Motohiko Ishida, Yusuke Mii, Noriyuki Kinoshita, Shinji Takada, Naoto Ueno, Satoshi Sawai, Yohei Kondo, and Kazuhiro Aoki. 2021. "Optogenetic Relaxation of Actomyosin Contractility Uncovers Mechanistic Roles of Cortical Tension during Cytokinesis." *Nature Communications* 12 (1): 1–13.

Yamamoto, Kei, Kohei Otomo, Tomomi Nemoto, Seiichiro Ishihara, Hisashi Haga, Akira Nagasaki, Yota Murakami, and Masayuki Takahashi. 2019. "Differential Contributions of Nonmuscle Myosin IIA and IIB to Cytokinesis in Human Immortalized Fibroblasts." *Experimental Cell Research* 376 (1): 67–76.

Yamazaki, Yosuke, Yuuri Miyata, Kenichi Morigaki, and Makito Miyazaki. 2024. "Controlling Physical and Biochemical Parameters of Actin Nucleation Using a Patterned Model Lipid Membrane." *Nano Letters* 24 (6): 1825–34.

Acknowledgments

We thank all members of the Miyazaki Laboratory for their helpful discussions and assistance. This work was supported by JSPS KAKENHI (Grant number 22J00094, 23K14179 to K.Y.; 21K19220, 22H05171 to M.M.), JST PRESTO (Grant number JPMJPR20ED to M.M.), RIKEN Incentive Research Project to K.Y. and RIKEN special postdoctoral researcher funding to K.Y. We appreciate Dr. François Robin and Dr. Kazuhiro Aoki for their fruitful advice and discussion.

Author contributions

K.Y. and M.M. designed the research. K.Y. performed experiments. K.Y. analyzed data. K.Y. and M.M. wrote the manuscript.

Competing Interests

The authors declare no competing interests.

935 **Figure Legends**

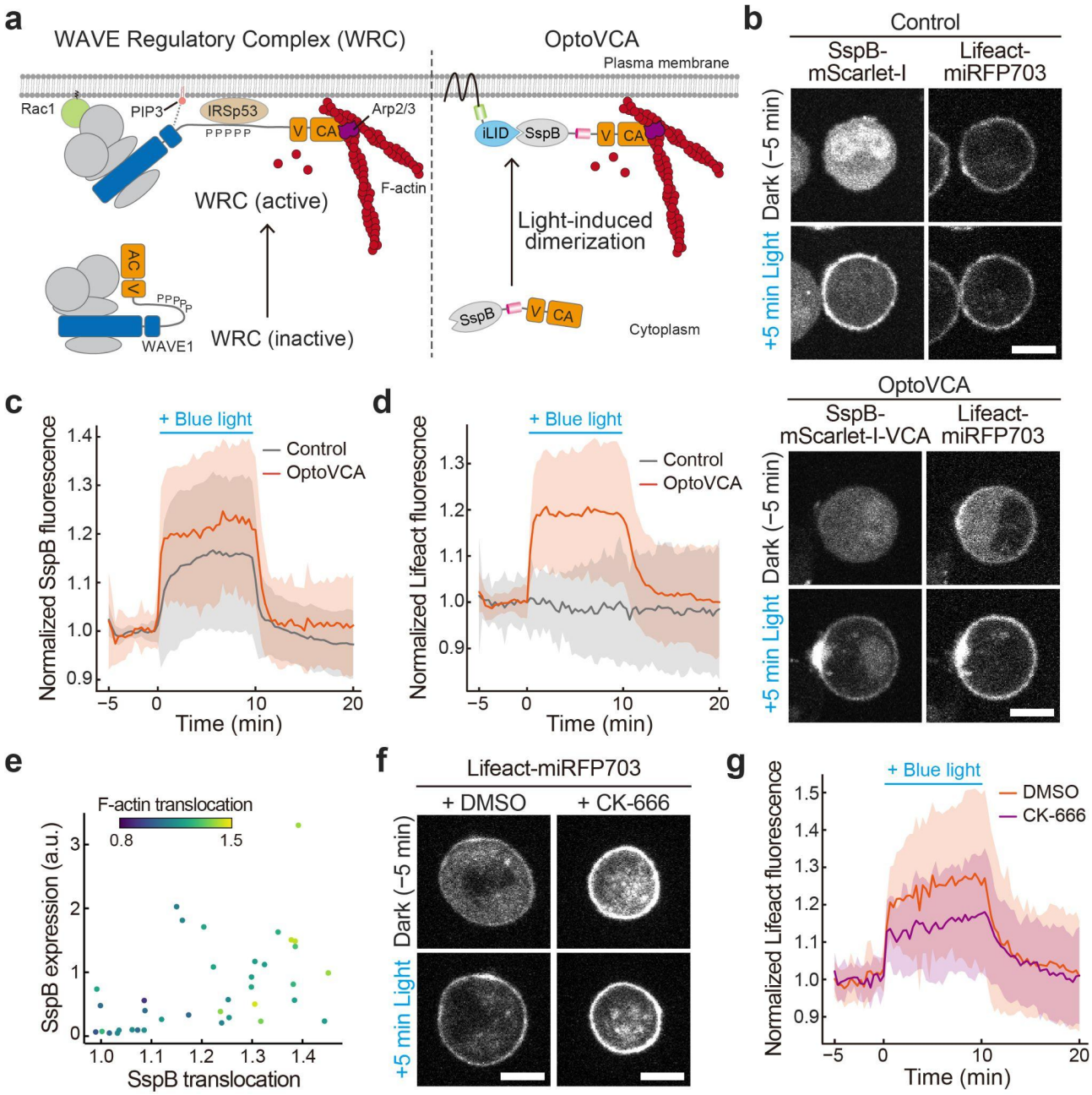

936

937 **Figure 1. Light-induced actin polymerization in live cells.** (a) Comparison of the regulatory
938 mechanisms of WRC (left) and OptoVCA system (right). (b) Representative images of MDCK cells
939 simultaneously expressing Stargazin-mEGFP-iLID and Lifeact-miRFP703 (right panels) along with
940 SspB-mScarlet-I (upper left) or SspB-mScarlet-I-VCA (lower left). For each cell, protein
941 localizations before (upper) and after (lower) blue light illumination are shown. (c, d) Normalized
942 cortical fluorescence intensity of SspB-mScarlet-I (c, Control) or SspB-mScarlet-I-VCA (c,
943 OptoVCA) and Lifeact-miRFP703 (d). The mean values (bold lines) are plotted as a function of time
944 with the SD. n = 37 for each cell. (e) Relationship between the translocation efficiency of SspB-
945 mScarlet-I-VCA and Lifeact-miRFP703, and the expression level of SspB-mScarlet-I-VCA. The
946 translocation efficiencies of SspB and F-actin are defined as the mean values of the normalized
947 fluorescence of SspB-mScarlet-I-VCA and Lifeact-miRFP703 at t = 2-8 min in (c) and (d),
948 respectively. n = 37 cells. (f) Representative images of the cells expressing Stargazin-mEGFP-iLID,
949 SspB-mScarlet-I-VCA, and Lifeact-miRFP703 treated with DMSO (left) or CK-666 (right) before
950 (upper) and after (lower) blue light illumination. (g) Normalized cortical fluorescence intensity of

951 Lifeact-miRFP703 in (f). The mean values (bold lines) are plotted as a function of time with the SD.
952 n = 18 and 17 for DMSO and CK-666 treated cells, respectively. All scale bars, 20 μm.

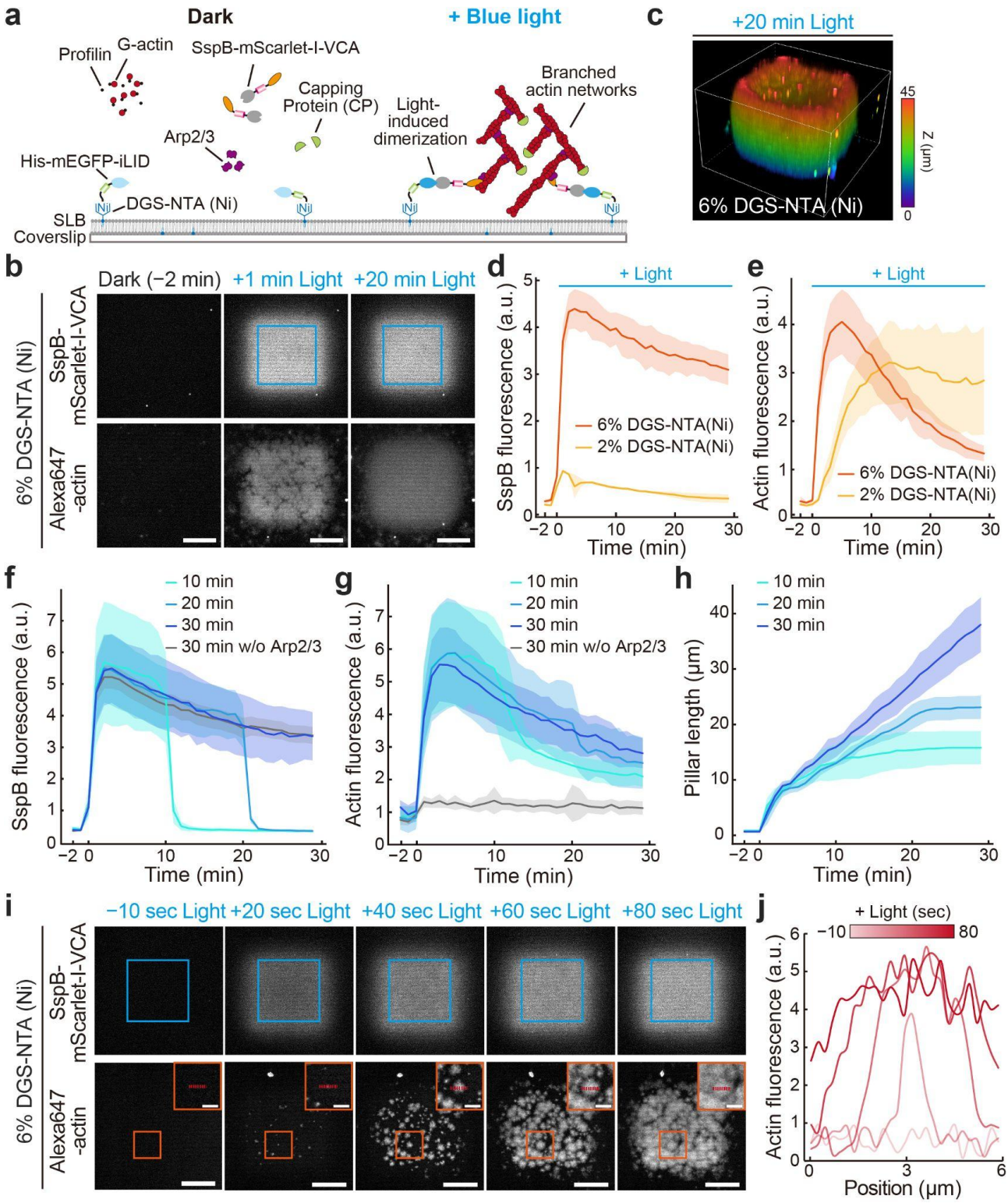

Figure 2. Light-induced actin polymerization on a supported lipid bilayer (SLB). (a) Schematic illustration of the OptoVCA system for *in vitro* experiments. Upon blue light illumination, actin polymerization is triggered by the recruitment of SspB-mScarlet-I-VCA to the SLB. Condition: 5 μM Actin, 15 μM Profilin, 100 nM Arp2/3, 25 nM CP, and 150 nM SspB-mScarlet-I-VCA. (b) Representative images of the recruitment of SspB-mScarlet-I-VCA (upper panels) and subsequent actin polymerization (lower panels) on 6% DGS-NTA(Ni) lipid at each indicated time point. Blue squares indicate the light-illuminated regions. All scale bars, 20 μm. (c) Three-dimensional reconstructed image of polymerized actin on 6% DGS-NTA(Ni) lipid after 20 min light illumination. (d, e) Fluorescence intensities of SspB-mScarlet-I-VCA (d) and Alexa647-actin (e) on 2% or 6%

963 DGS-NTA(Ni) lipid. The mean values (bold lines) are plotted as a function of time with the SD. *n* =
964 12 for each condition. (f, g, h) Fluorescence intensities of SspB-mScarlet-I-VCA (f) and Alexa647-
965 actin (g), and the pillar length (h) in each indicated illumination duration (f, g, h) and for the condition
966 without Arp2/3 (f, g). The mean values (bold lines) are plotted as a function of time with the SD. *n* =
967 12 for each condition. (i) High-speed imaging of the recruitment of SspB-mScarlet-I-VCA (upper
968 panels) and subsequent actin polymerization (lower panels) on 6% DGS-NTA(Ni) lipid. Blue-
969 squared regions were illuminated at 10 sec intervals. Orange-squared regions in the lower panels are
970 magnified and shown as the inset images. Scale bars, 20 μm and 5 μm for the wide-view images and
971 the inset images, respectively. (j) Growth dynamics of a single actin network seed quantified by the
972 line scan along red dashed lines in the inset images of (i).

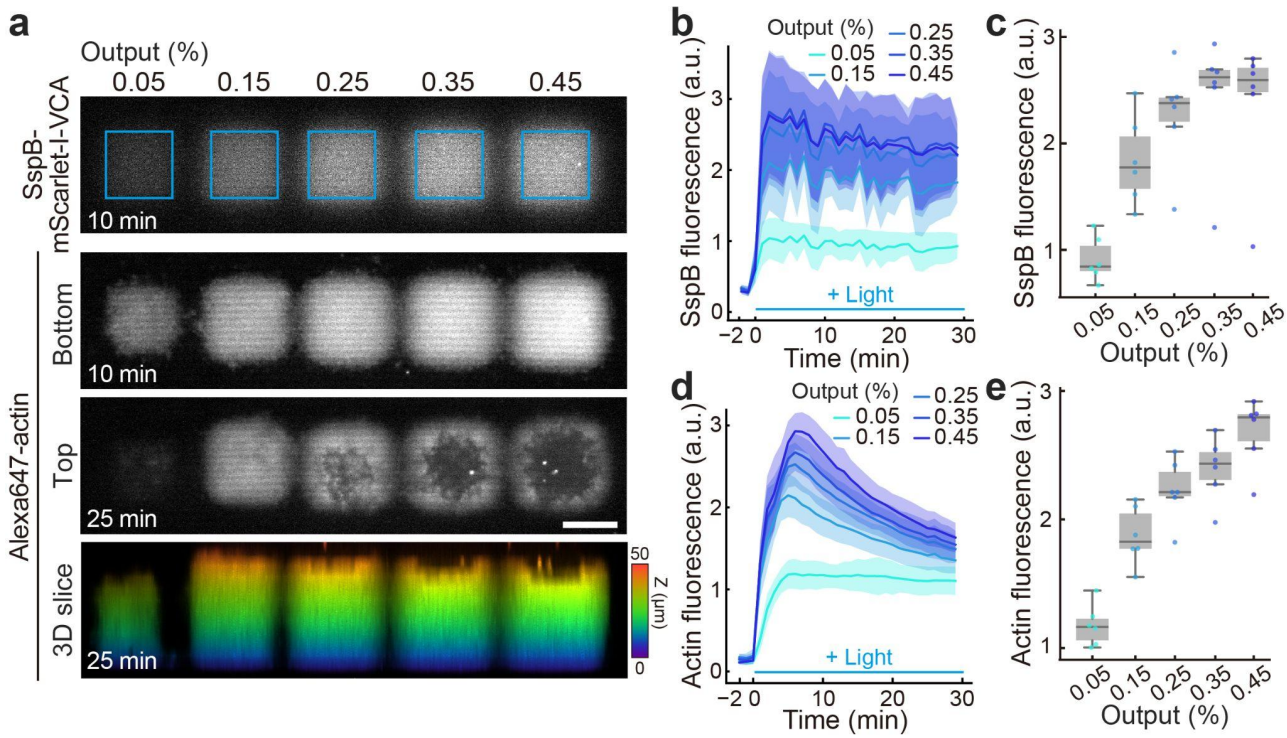

Figure 3. Control of actin density by light intensity. (a) Representative images of the recruitment of SspB-mScarlet-I-VCA (upper panel) and subsequent actin polymerization (lower panels) under five different light-powered illuminations on 6% DGS-NTA(Ni) lipid. The bottom plane, top plane, and three-dimensional(3D) reconstructed slice images at each indicated time point are shown. Condition: 5 μM Actin, 15 μM Profilin, 100 nM Arp2/3, 25 nM CP, and 150 nM SspB-mScarlet-I-VCA. Blue squares indicate the illuminated regions. (b, c) Fluorescence intensities of SspB-mScarlet-I-VCA under the five different light-powered illuminations. For box plots in (c), the mean fluorescence intensities of SspB-mScarlet-I-VCA at t = 11-20 min in (b) are used. (d, e) Fluorescence intensities of Alexa647-actin with five different light-powered illuminations. For box plots in (e), the fluorescence intensities of Alexa647-actin at t = 10 min in (d) are used. (b, d) The mean values (bold lines) are plotted as a function of time with the SD. n = 6 for each condition.

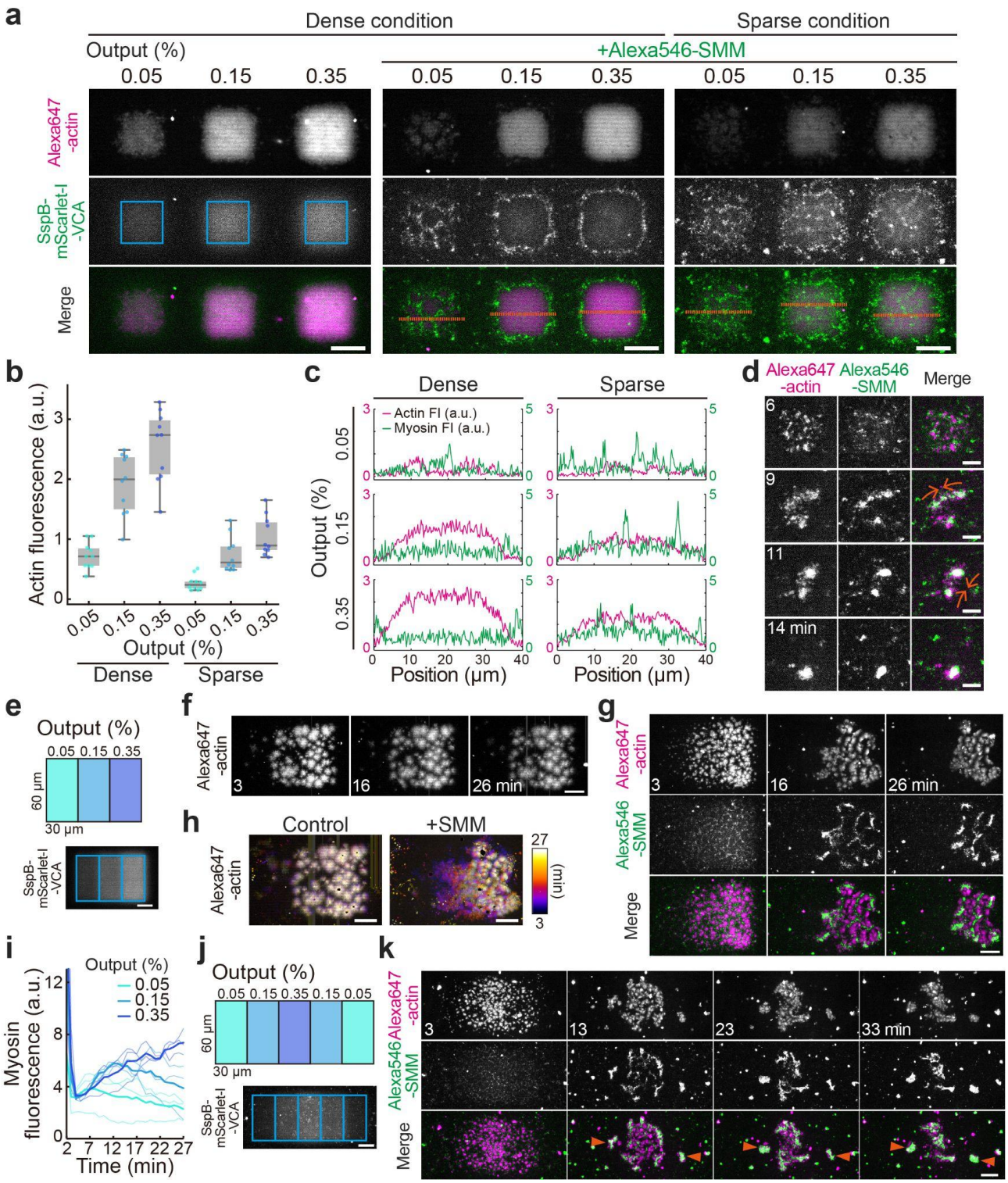

Figure 4. Actin density-dependent myosin penetrations and flows. (a) Representative images of polymerized actin (upper panels) and SspB-mScarlet-I-VCA (middle panels) in the absence of (left column) or the presence of 200 nM Alexa546-SMM (middle and right columns). Dense condition: 5 μM Actin, 15 μM Profilin, 100 nM Arp2/3, 25 nM CP, and 150 nM SspB-mScarlet-I-VCA. Sparse condition: 2 μM Actin, 6 μM Profilin, 100 nM Arp2/3, 10 nM CP, and 150 nM SspB-mScarlet-I-VCA. Images taken after 5 min illumination are shown. Blue squares indicate the illuminated regions. (b) Box plots of the fluorescence intensities of actin 2 μm above SLB after 5 min illumination. n = 10 for each condition. (c) Line profiles of the actin and myosin intensities along the orange dashed lines shown in (a). (d) Representative images of the movements of actin and myosin puncta. Blue light was illuminated for 5 min from t = 0 to 5 min. The elapsed times are indicated in the images of

Alexa647-actin. Orange arrows indicate the direction of the puncta movements. (e) Illumination pattern to induce actin flow (upper) and the fluorescence image of recruited SspB-mscarlet-I-VCA (lower). (f, g) Maximum intensity projection images of the actin structure produced by the illumination pattern shown in (e) in the absence (f) or the presence of 200 nM Alexa546-SMM (g). The SMM signal is shown in middle panels in (g). The protein concentrations are identical to the sparse network in (a). Blue light was illuminated for 2 min from $t = 0$ to 2 min. The elapsed times are indicated in the images of Alexa647-actin. (h) Temporal color-coded images of the actin structure in (f, g) after stopping the illumination. (i) Fluorescence intensities of Alexa546-SMM in the three regions shown in (e) after stopping the illumination. The bold lines indicate the mean values of three independent experiments (thin lines). (j) Illumination pattern to induce actin flow from both sides (upper) and the fluorescence image of recruited SspB-mscarlet-I-VCA (lower). (k) Maximum intensity projection images of the actin and SMM structures produced by the illumination pattern shown in (j). Blue light was illuminated for 2 min from $t = 0$ to 2 min. The elapsed times are indicated in the images of Alexa647-actin. Orange arrowheads indicate disconnected actin structures in the sparse regions. Scale bars, 20 μm and 10 μm for (a, e, f, g, h, j, k) and (d), respectively.

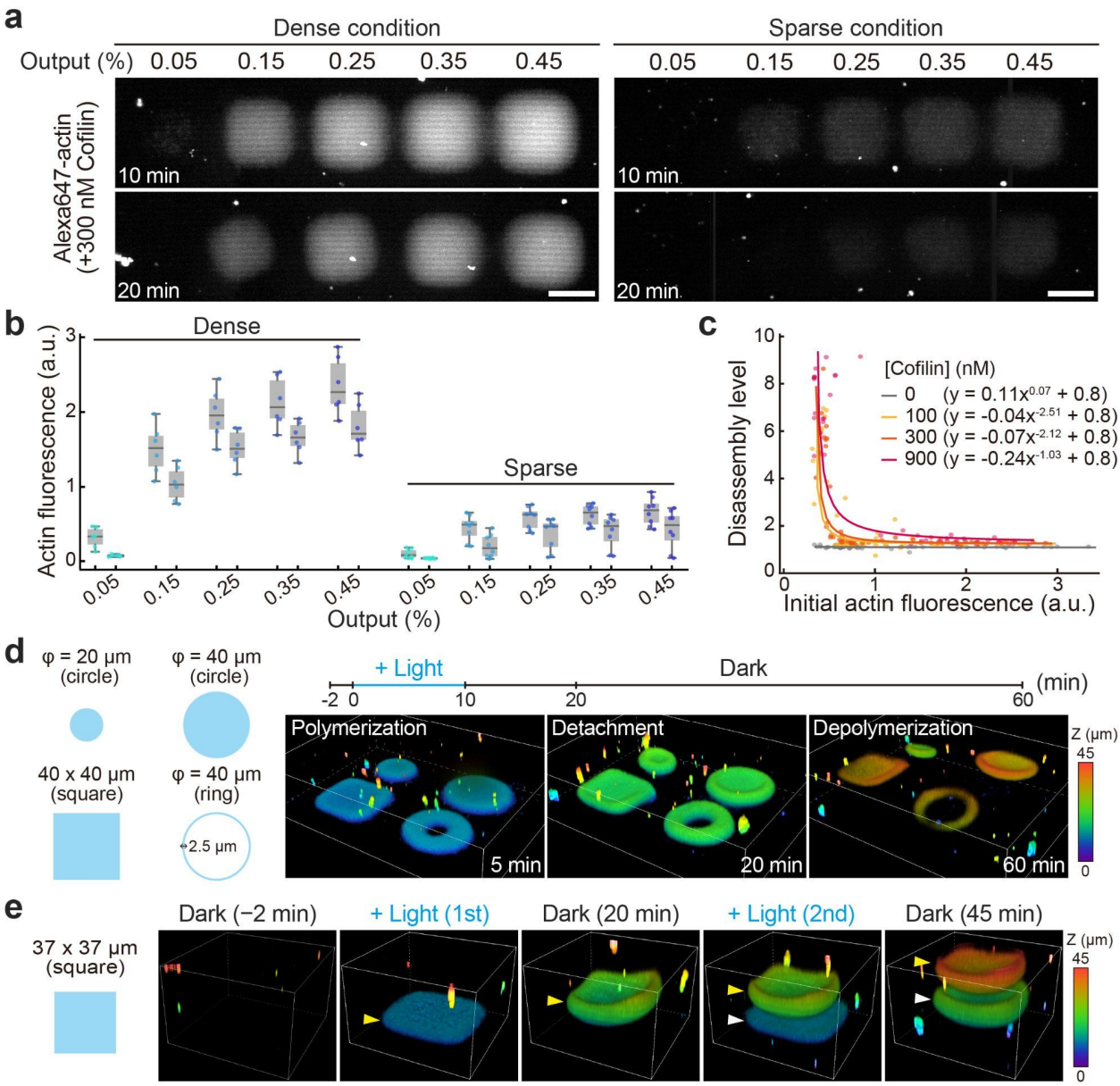

Figure 5. Effects of cofilin on various actin densities. (a) Maximum intensity projection images of actin networks after 10 min illumination (upper panels) and 10 min after stopping the illumination (lower panels). Dense condition: 5 μM Actin, 15 μM Profilin, 50 nM Arp2/3, 25 nM CP, 150 nM SspB-mScarlet-I-VCA, and 300 nM Cofilin. Sparse condition: 2 μM Actin, 6 μM Profilin, 50 nM Arp2/3, 10 nM CP, 150 nM SspB-mScarlet-I-VCA, and 300 nM Cofilin. All scale bars, 20 μm. (b) Box plots of the fluorescence intensities of Alexa647-actin after 10 min illumination (left boxes) and 10 min after stopping the illumination (right boxes) in the presence of 300 nM cofilin. n = 6 and 8 for dense and sparse conditions, respectively. (c) Relationship between the initial fluorescence intensity of Alexa647-actin and the actin disassembly level. The disassembly level was calculated by dividing the intensity 10 min after illumination by the intensity 10 min after stopping the illumination. Bold lines indicate power-law fitting. n = 51, 60, 57, 42 for 0, 100, 300, 900 nM Cofilin, respectively. (d) Three-dimensional reconstructed images of floating actin networks on 6% DGS-NTA(Ni) lipid at each indicated time point produced by various illumination patterns. (e) Three-dimensional reconstructed images of floating actin networks by a square-shaped illumination pattern on 6% DGS-NTA(Ni) lipid at each indicated time point. Yellow and white arrowheads indicate the first and second polymerization, respectively. (d, e) Condition: 5 μM Actin, 15 μM Profilin, 100 nM Arp2/3, 25 nM CP, 150 nM SspB-mScarlet-I-VCA, and 600 nM Cofilin.

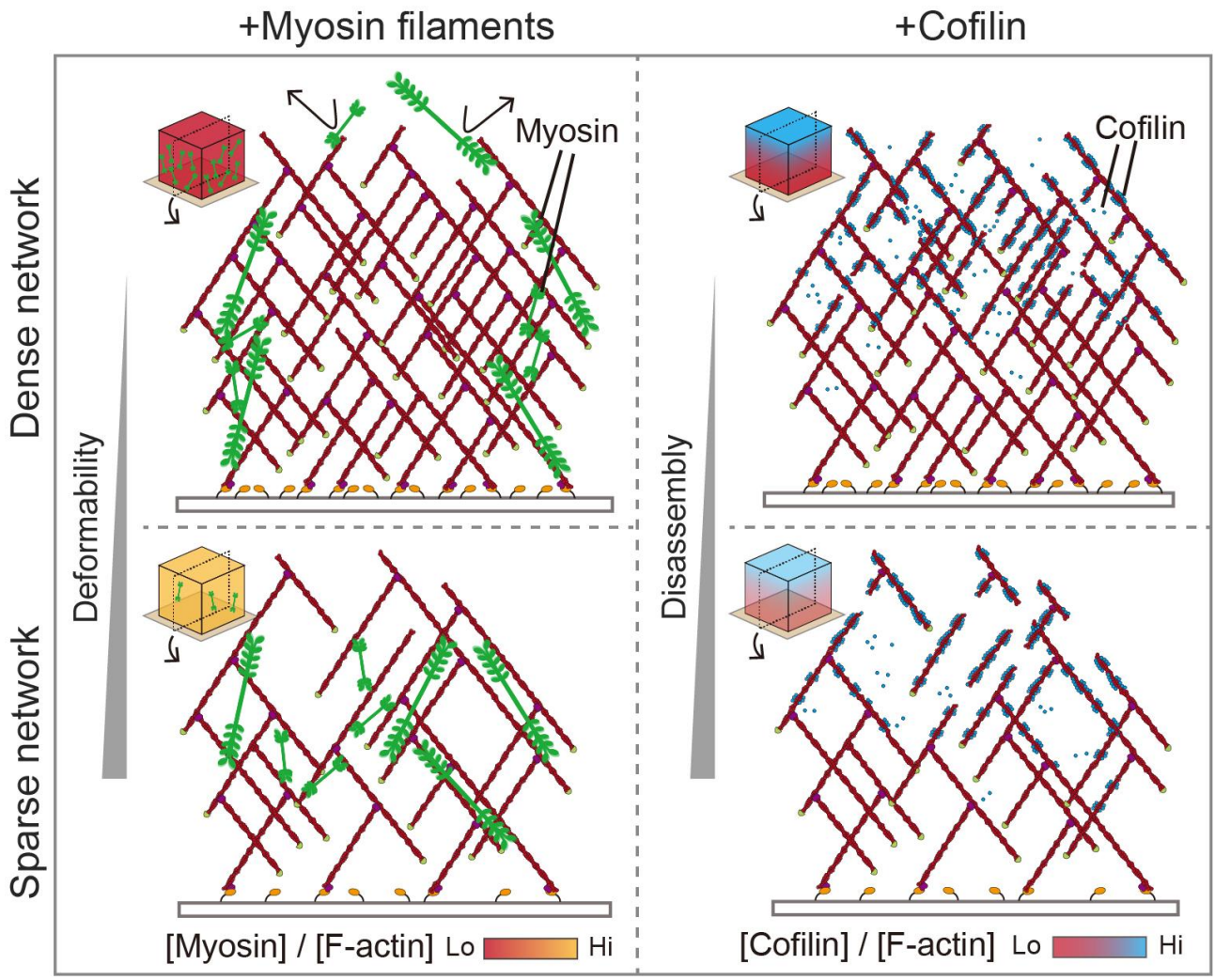

Figure 6. Actin network density-dependent protein penetrations and functions. Schematic illustration showing the overhead view and side view of assembled actin networks in the presence of myosin filaments (left) and cofilin (right). The color bars indicate the proportion of myosin and cofilin bound to actin filaments within the network. Myosin: In the dense network, myosin filaments cannot penetrate into the network and are trapped at the side surface due to the steric hindrance (upper left). Myosin filaments cannot stay longer on the top surface. In the sparse network, myosin filaments can penetrate into the network with the help of motor activity and the penetration makes the network deformable (lower left). Cofilin: cofilin can penetrate into both the sparse and the dense networks and preferentially binds to ADP-actin. In the dense network, the network disassembly rate is low (upper right). In the sparse network, cofilin-mediated network disassembly is more active (lower right).

1040 **Supplementary Information**

1041

1042

1043 Optogenetic actin network assembly on lipid bilayer uncovers the network 1044 density-dependent functions of actin-binding proteins.

1045

1046

1047 **Author list**

1048 Kei Yamamoto[1*], and Makito Miyazaki[1,2,3*]

1049

1050

1051 **Affiliations**

1052 [1]RIKEN Center for Biosystems Dynamics Research, 1-7-22 Suehiro-cho, Tsurumi-ku, Yokohama
1053 230-0045, Japan.

1054 [2]Graduate School of Medicine, Science and Technology, Shinshu University, 3-1-1 Asahi,
1055 Matsumoto, Nagano 390-8621, Japan.

1056 [3]PRESTO, JST, 4-1-8 Honcho, Kawaguchi, Saitama, 332-0012, Japan.

1057 *Correspondence: kei.yamamoto.jv@riken.jp and makito.miyazaki@riken.jp

1058 ## Supplementary Note

1059 **Estimation of the actin network density from fluorescence images**

1060 To estimate the density of the actin networks assembled by illumination, we first measured the
1061 fluorescence intensity of homogeneous F-actin solutions with known concentrations. Briefly, 90 μM
1062 actin (10 mol % labeled with Alexa647) was polymerized in a polymerization buffer containing 50
1063 mM KCl, 1 mM $MgCl_2$, 1 mM EGTA, 20 mM 2-mercaptoethanol, 1 mg/mL BSA, 1 mM ATP, and
1064 20 mM HEPES (pH7.2) at 25 °C for 30 min (Shrivastava et al. 2015). During polymerization, the
1065 SLB was formed in a hand-made flow cell. To minimize the effect of the background signal from out
1066 of focus, we made a thin flow cell using two pieces of plastic wrap as a spacer. The thickness
1067 measured by a microscope was 12.75 ± 2.25 μm, which was comparable to the height of actin
1068 structures assembled by illumination. The polymerized actin solution was serially diluted with the
1069 polymerization buffer and loaded into the flow cells. The fluorescence intensities of F-actin solutions
1070 4 μm above the glass surface were measured and plotted (Fig. S6c).

1071 Next, we compared the fluorescence intensities of F-actin solutions with light-induced actin
1072 networks. We simply compared the raw fluorescence intensities of the F-actin solutions and pillars
1073 without subtracting the background noise. This is because the rolling ball subtraction method is not
1074 suitable for nearly homogeneous images, such as those of F-actin solutions. The concentrations of
1075 the actin networks in the sparse conditions, the dense conditions with 0.05-0.15% outputs, and the
1076 dense conditions with 0.15-0.45% outputs are estimated to be 0-20, 20-40, and 40-60 μM,
1077 respectively.

1078 Assuming that the concentration of the densest network is ~50 μM, the density of actin
1079 molecules is 30,000/μm^3. It can be reasonably approximated that actin filaments are uniformly
1080 distributed in the pillar and extend vertically from the SLB (Yamazaki et al. 2024). Given that an
1081 actin filament elongates by 2.7 nm in length with each binding of actin monomers (Kubota et al.
1082 2018), the number of actin molecules in each filament is ~370 molecules per μm along the Z-axis.
1083 Therefore, the density of actin filaments in the XY plane is estimated to be ~81 filaments/μm^2. This
1084 corresponds to 9 filaments per μm, meaning that the filaments are spaced ~110 nm apart on average.
1085 Applying the same estimation method to the actin networks at a density of 25 μM, which allows
1086 myosin penetration into the network (Fig. 4a, S6c), results in ~160 nm apart on average.

1087

1088

1089 **Estimation of the actin filament length**

1090 The length of branched actin filaments is determined by the competitive binding of actin monomers
1091 and capping protein (CP) to the barbed end of an elongating filament. Therefore, the length

distribution of branched filaments can be estimated from the association rate constants of ATP-actin and capping protein to the barbed end. The probability of the binding of CP to a filament after the polymerization of n actin molecules can be expressed as

$$p(n) = {p_\mathrm{a}}^n p_\mathrm{c}\,,$$

where the binding probabilities of actin monomer and CP are given as $p_\mathrm{a} = k_\mathrm{on}^\mathrm{a}[\mathrm{actin}]/C$ and $p_\mathrm{c} = k_\mathrm{on}^\mathrm{c}[\mathrm{CP}]/C$, respectively, and $C = k_\mathrm{on}^\mathrm{a}[\mathrm{actin}] + k_\mathrm{on}^\mathrm{c}[\mathrm{CP}]$ is the normalization constant. By substituting the literature values (k_on^a = 12 μM^{-1} s^{-1} (Pollard 2016), k_on^c = 3-6 μM^{-1} s^{-1} (Schafer et al. 1996; Wear et al. 2003)) and the concentrations used for the experiments ([actin] = 5 μM, [CP] = 0.025 μM), the expected value of n is calculated as

$$E = \sum_{n=1}^{\infty} n\, p(n)/C^* \approx 400\sim800,$$

where C^* is the normalization constant represented as

$$C^* = \sum_{n=1}^{\infty} p(n).$$

Given that an actin filament elongates by 2.7 nm with each binding of actin monomers (Kubota et al. 2018), the expected filament length is approximately 1-2 μm. Note that the filament length was estimated to be ~300 nm in the actin pillars assembled from similar protein compositions to our experiments (Bieling et al. 2016). Given that the concentration of capping protein is 4 times lower in our experiments, the potential filament length estimated from the previous study would be ~1,200 nm. This value is also consistent with our estimation.

Supplementary Figures

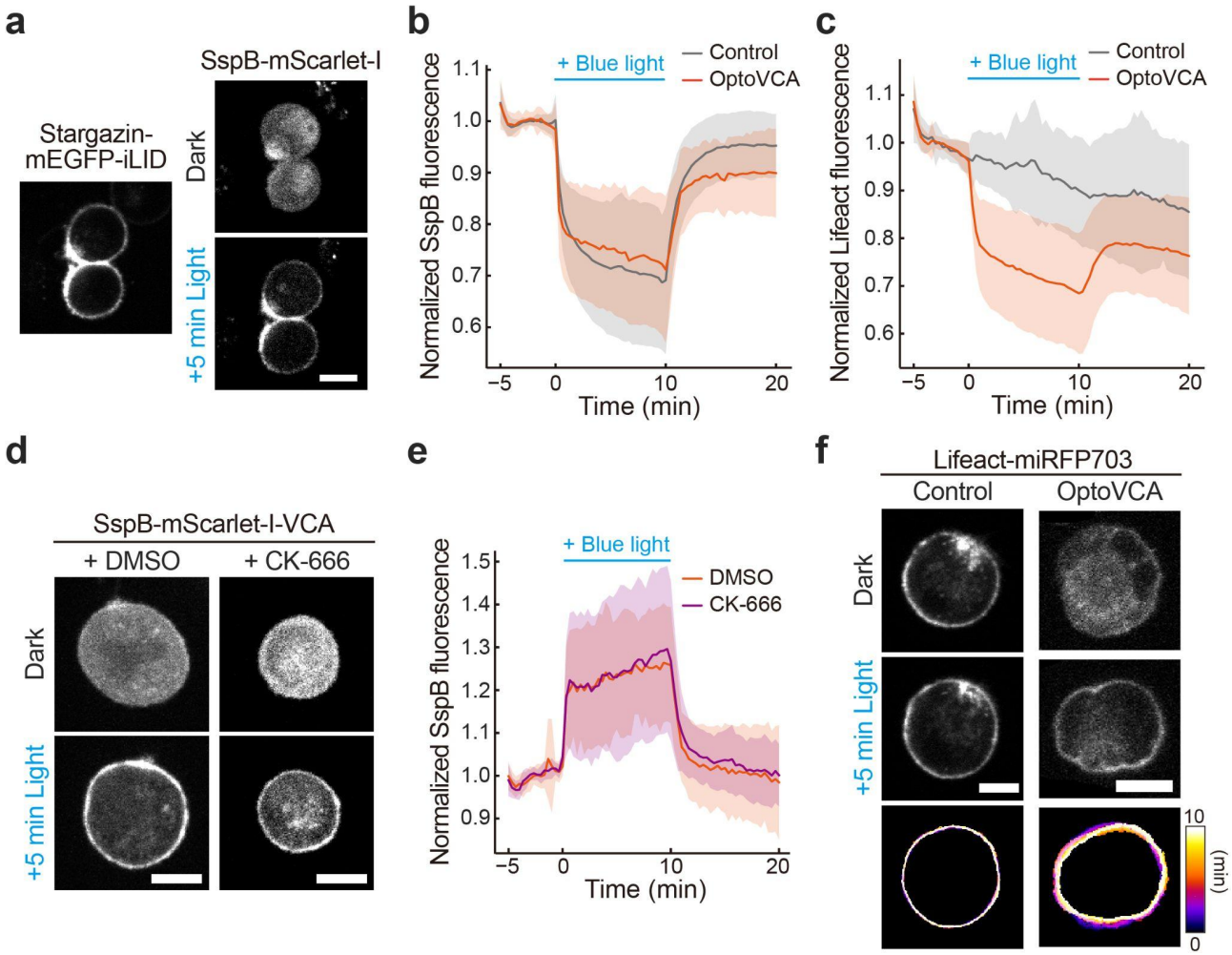

Figure S1. OptoVCA system for *in vivo* experiments. (a) Representative images of MDCK cells expressing Stargazin-mEGFP-iLID (left) and SspB-mScarlet-I (right). Upon blue light illumination, SspB-mScarlet-I translocated from the cytoplasm to the plasma membrane. (b) The normalized cytoplasmic fluorescence intensity of SspB-mScarlet-I (Control) or SspB-mScarlet-I-VCA (OptoVCA). The mean values (bold lines) are plotted as a function of time with the SD. $n = 37$ cells. (c) The normalized cytoplasmic fluorescence intensity of Lifeact-miRFP703. The mean values (bold lines) are plotted as a function of time with the SD. $n = 37$ cells. (d) Representative images of the cells expressing SspB-mScarlet-I-VCA treated with DMSO (left) or CK-666 (right) before (upper) and after (lower) blue light illumination. (e) Normalized cortical fluorescence intensity of SspB-mScarlet-I-VCA treated with DMSO or CK-666. The mean values (bold lines) are plotted as a function of time with the SD. $n = 18$ and 17 for DMSO and CK-666 treated cells, respectively. (f) Comparison of shape changes between control cell (left) and OptoVCA expressing cells (right). Temporal color-coded images show the cell edges after starting illumination. All scale bars, 20 μm.

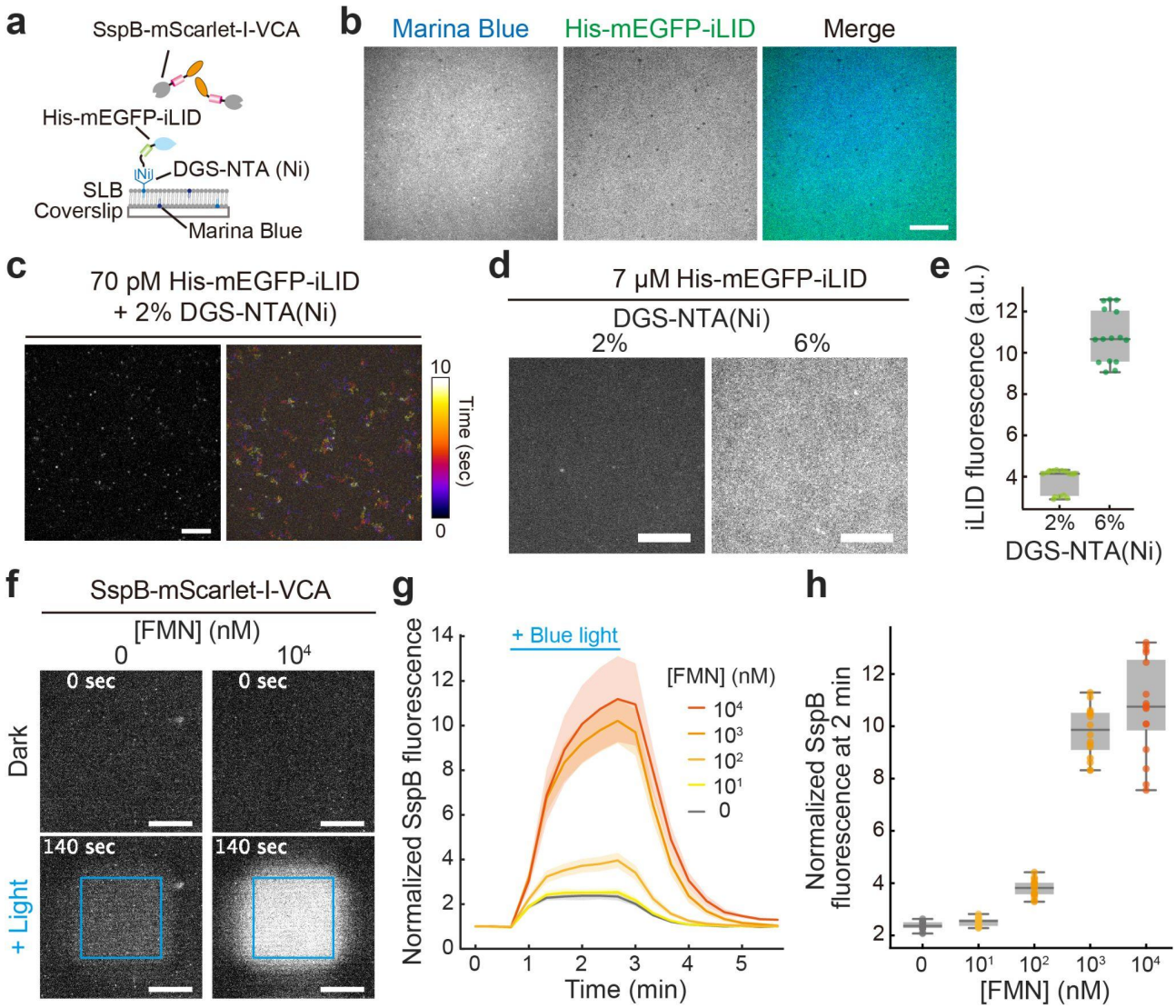

Figure S2. Optimization of iLID-SspB system for *in vitro* experiments. (a) Schematic illustration of the OptoVCA system without cytoskeletal proteins. (b) Representative images of SLB visualized by 2% Marina Blue lipid. 6% DGS-NTA(Ni) was added to POPC to anchor His-mEGFP-iLID on SLB. (c) TIRF images of lipid-bound His-mEGFP-iLID. Left, a single snapshot. Right, a temporal color-coded image reconstructed from 100 images taken over 10 sec. (d) Representative images of His-mEGFP-iLID on SLB containing 2% (left) or 6% (right) DGS-NTA(Ni). (e) Fluorescence intensities of His-mEGFP-iLID in (d). $n = 15$ for each sample. (f) Representative images showing the accumulation of SspB-mScarlet-I-VCA on SLB before (upper) and after (lower), and without FMN (left) and with 10^4 nM of FMN. Condition: 150 nM SspB-mScarlet-I-VCA. Blue-squared regions were illuminated. (g) Fluorescence intensities of SspB-mScarlet-I-VCA in the presence of various concentrations of FMN. The mean values (bold lines) are plotted as a function of time with the SD. (h) Fluorescence intensities of SspB-mScarlet-I-VCA at $t = 2$ min in (g). $n = 16$ for each sample. All scale bars, 20 μm.

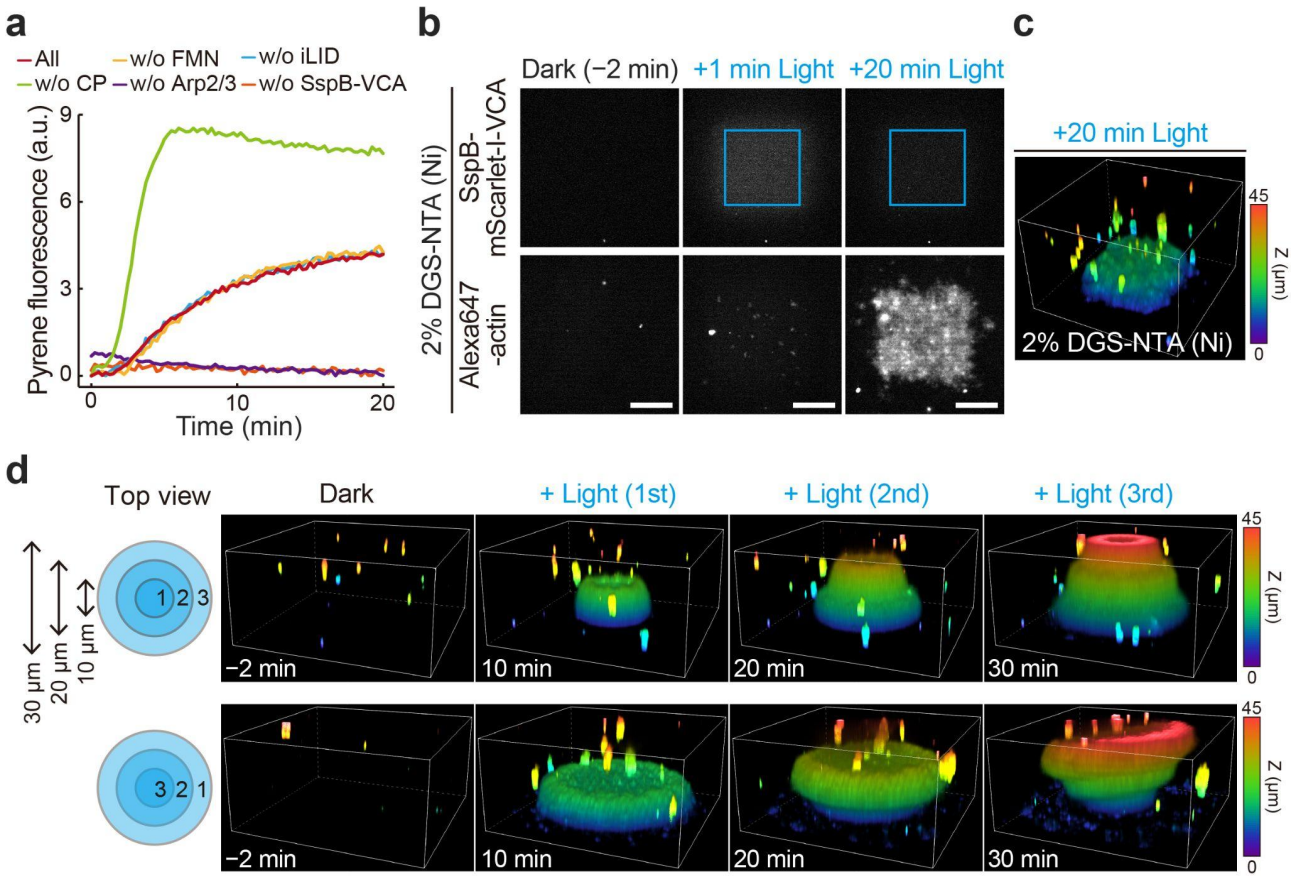

Figure S3. Optimization and validation of *in vitro* OptoVCA system. (a) Pyrene fluorescence assay using all components or omitting each component to confirm actin polymerization activity. (b) Representative images showing the recruitment of SspB-mScarlet-I-VCA (upper panels) and subsequent actin polymerization (lower panels) on 2% DGS-NTA(Ni) lipid. The illuminated regions are indicated by blue squares. All scale bars, 20 μm. (c) Three-dimensional reconstructed image of polymerized actin on 2% DGS-NTA(Ni) lipid after 20 min of illumination. (d) Schematic illustration of the three-step illumination process (left) and representative images of the created actin structures (right). Each indicated region was illuminated for 10 min in the order specified by the numbers in the illustration. Condition: 5 μM Actin, 15 μM Profilin, 100 nM Arp2/3, 25 nM CP, and 150 nM SspB-mScarlet-I-VCA.

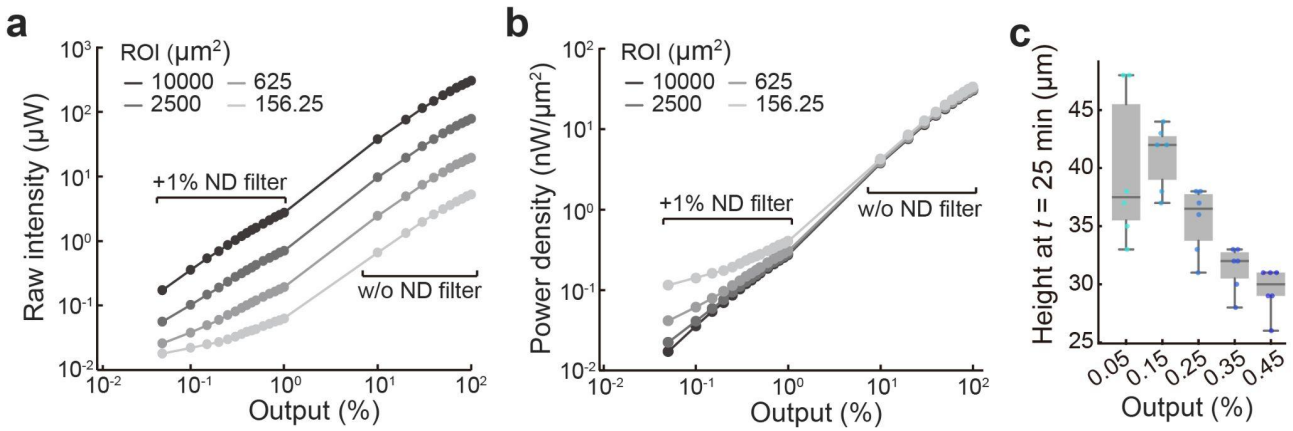

Figure S4. Control of actin density by light intensity. (a,b) Raw light intensities with different-sized illumination patterns (a) and the power densities normalized by the illuminated areas (b) plotted as a function of the output power of the DMD light source. (c) Heights of actin pillars in Fig. 3 at t = 25 min. n = 6 for each condition.

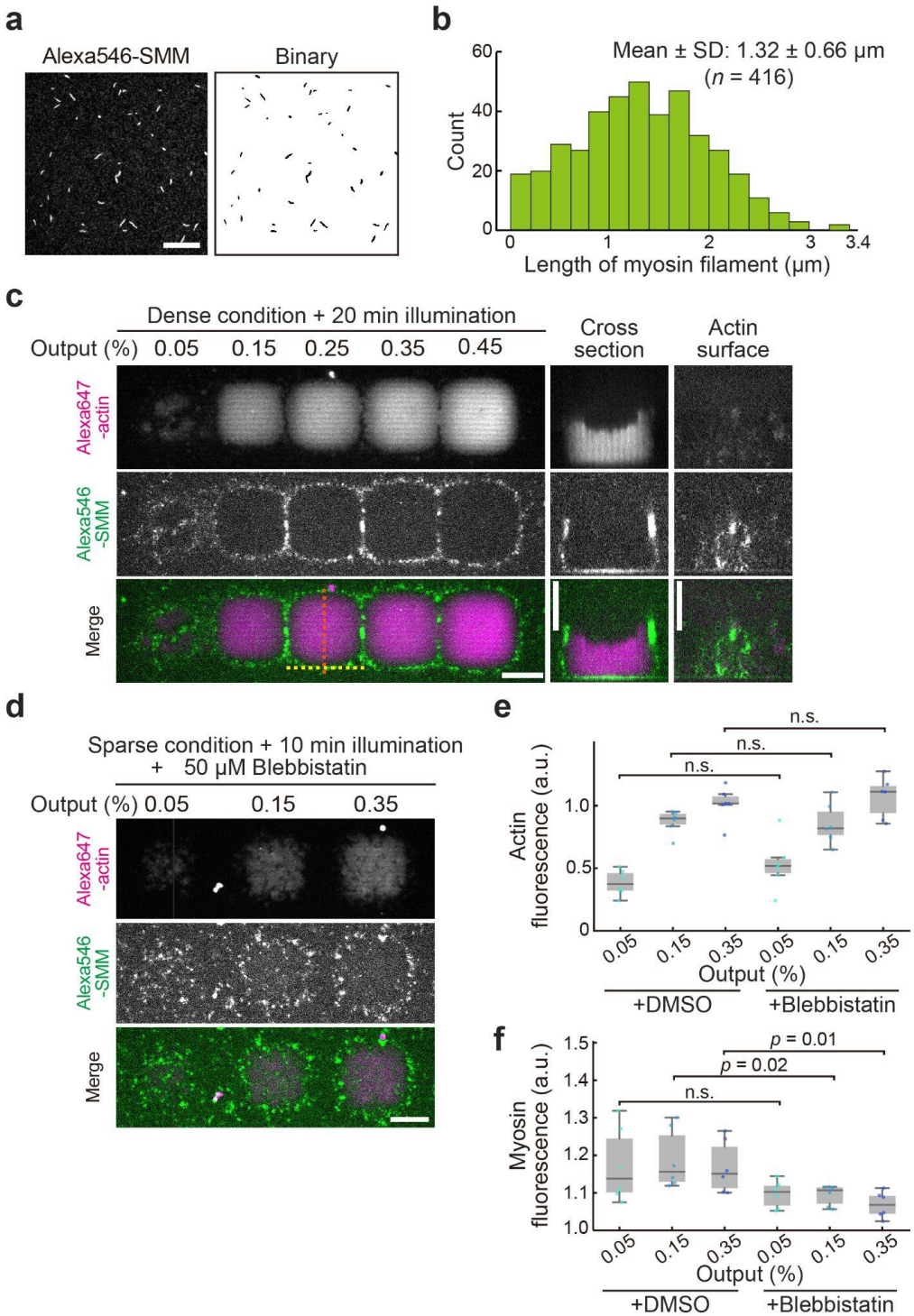

Figure S5. Effects of actin network density on myosin. (a) Myosin filaments labeled with Alexa546 (left) and its binarized image (right). Scale bar, 10 μm. (b) Histogram showing the length distribution of myosin filaments. (c) Spatial distribution of SMM in dense conditions. The cross-section and actin surface images correspond to the orange and yellow dashed lines in the merged image, respectively. Condition: 5 μM Actin, 15 μM Profilin, 100 nM Arp2/3, 25 nM CP, 150 nM SspB-mScarlet-I-VCA, and 200 nM Alexa546-SMM. All scale bars, 20 μm. (d) Spatial distribution of SMM treated with 50 μM blebbistatin in the sparse condition. Condition: 2 μM Actin, 6 μM Profilin, 100 nM Arp2/3, 10 nM CP, 150 nM SspB-mScarlet-I-VCA, and 200 nM Alexa546-SMM. Scale bar, 20 μm. (e, f) Fluorescence intensities of actin (e) and myosin (f) in the sparse condition. *p* values were calculated by unpaired *t*-test. $n = 6$ for each sample.

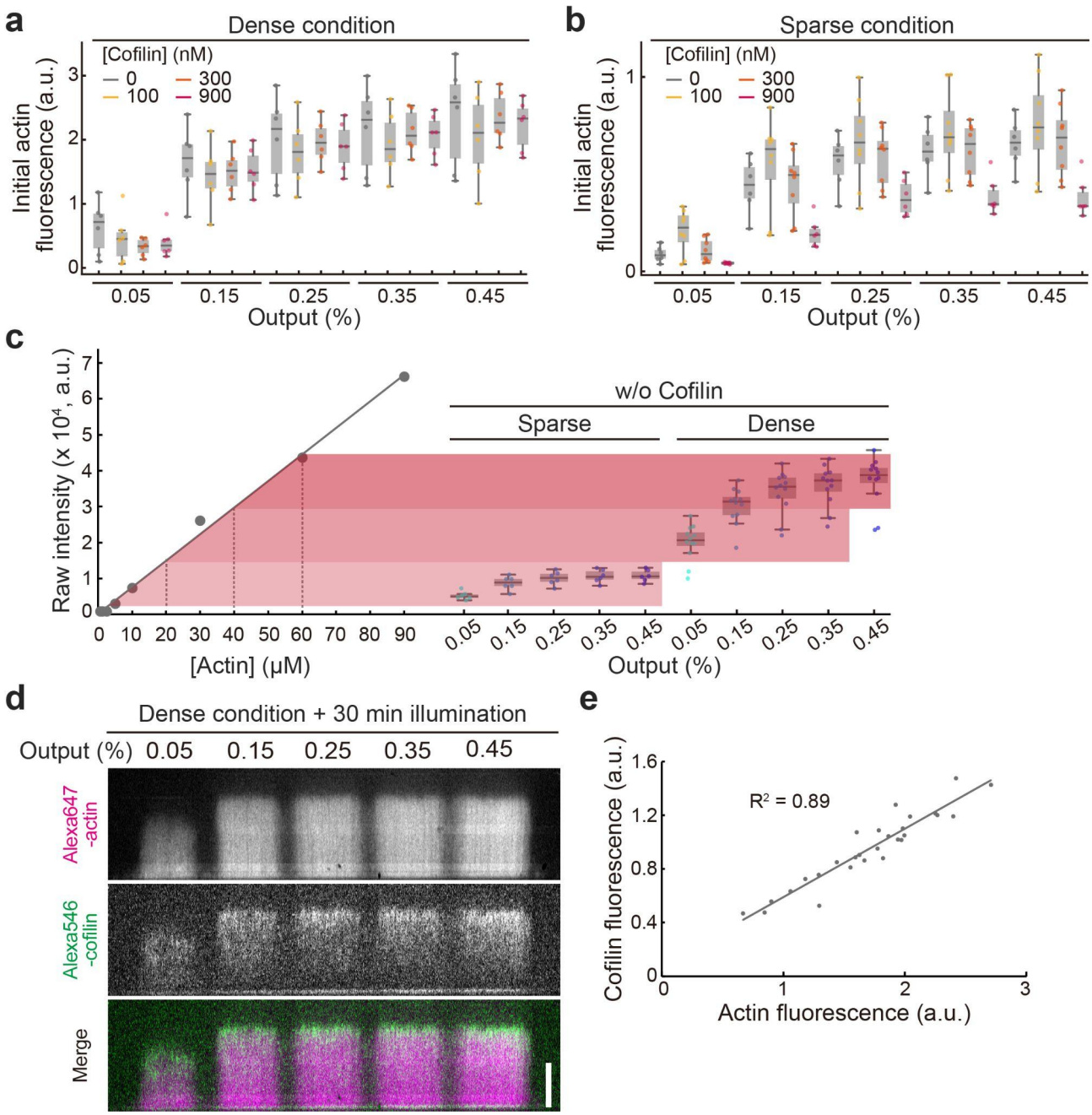

Figure S6. Effects of actin network density on cofilin. (a, b) Initial actin fluorescence intensities in the dense (a) and sparse (b) conditions after 10 min illumination. In the dense conditions, n = 6 for each cofilin concentration. In the sparse conditions, n = 6, 8, 8, 6 for 0, 100, 300, 900 nM cofilin, respectively. (c) Comparison of the raw fluorescence intensities between homogeneous F-actin solutions (left) and light-induced actin networks (right). n = 6 and 12 for sparse and dense conditions, respectively. (d) Spatial distribution of cofilin in the dense condition. Condition: 5 μM Actin, 15 μM Profilin, 100 nM Arp2/3, 25 nM CP, 150 nM SspB-mScarlet-I-VCA, and 900 nM Alexa546-cofilin. Scale bar, 20 μm. (e) Relationship between the fluorescence intensities of actin and cofilin in single actin networks. n = 28 from individual actin networks.

Supplementary Movie legends

Movie S1. Growth dynamics of actin networks induced by three-step illumination patterns.

Movie S2. Growth dynamics of actin network seeds upon blue light illumination. The blue rectangular region indicates the illuminated area. Scale bar, 20 μm.

Movie S3. Growth dynamics of actin pillars induced by five different illumination intensities.

Movie S4. Formation of an actin sheet with a density gradient, followed by SMM-driven actin flow toward the dense region. Blue rectangular regions indicate illuminated areas. Scale bar, 20 μm.

Movie S5. Formation of an actin sheet with a density gradient, followed by SMM-driven actin flow from both sides toward the central dense region. Blue rectangular regions indicate illuminated areas. Scale bar, 20 μm.

Movie S6. Floating actin networks induced by various illumination patterns.

Movie S7. Floating actin networks induced by repetitive illuminations.